

# Early-time jet formation in liquid-liquid impact problems: theory and simulations

R. CIMPEANU<sup>1,2</sup> AND M. R. MOORE<sup>1</sup>

<sup>1</sup> Mathematical Institute, Andrew Wiles Building, Radcliffe Observatory Quarter, Woodstock Road, Oxford, OX2 6GG, UK,

<sup>2</sup> Department of Mathematics, Imperial College London, South Kensington Campus, London, SW7 2AZ, UK.

(Received ?; revised ?; accepted ?. - To be entered by editorial office)

We perform a thorough qualitative and quantitative comparison of theoretical predictions and direct numerical simulations for the two-dimensional, vertical impact of two droplets of the same fluid. In particular, we show that the theoretical predictions for the location and velocity of the jet root are excellent in the early stages of the impact, while the predicted jet velocity and thickness profiles are also in good agreement with the computations before the jet begins to bend.

By neglecting the role of the surrounding gas both before and after impact, we are able to use Wagner theory to describe the early-time structure of the impact. We derive the model for general droplet velocities and radii, which encompasses a wide range of impact scenarios from the symmetric impact of identical drops to liquid drops impacting a deep pool. The leading-order solution is sufficient to predict the curve along which the root of the high-speed jet travels. After moving into a frame fixed in this curve, we are able to derive the zero-gravity shallow-water equations governing the leading-order thickness and velocity of the jet.

Our numerical simulations are performed in the open-source software *Gerris*, which allows for the level of local grid refinement necessary for a problem with such a wide variety of lengthscales. The numerical simulations incorporate more of the physics of the problem, in particular the surrounding gas, the fluid viscosities, gravity and surface tension. We compare the computed and predicted solutions for a range of droplet radii and velocities, finding excellent agreement in the early stage. In light of these successful comparisons, we discuss the tangible benefits of using Wagner theory to confidently track properties such as the jet root location, jet thickness and jet velocity in future studies of splash jet/ejecta evolution.

**Key words:** Authors should not enter keywords on the manuscript, as these must be chosen by the author during the online submission process and will then be added during the typesetting process (see <http://journals.cambridge.org/data/relatedlink/jfm-keywords.pdf> for the full list)

---

## 1. Introduction

Impact problems are widespread throughout real-world phenomena and industrial processes and occur on a multitude of scales. On the large scale, ship-slamming involves a large solid body crashing into the ocean, so that the key question is to determine the force felt on the body as it slams. On a smaller scale, the impact of liquid drops onto solids or liquids has a variety of applications including inkjet printing, coating processes,

agricultural and industrial sprays, and understanding soil erosion. In such scenarios, the evolution of the ejecta/splash jet is often the pertinent flow feature.

Rapid topological changes on small lengthscales make impact problems a challenge analytically, numerically and experimentally, so that in order to gain an understanding of the problem, each field must complement the others. Recent advances in numerical and experimental capabilities have allowed us a deeper insight into the early stages of droplet impact in particular, although the mathematical principles can be extended to solid impact as well. Yarin (2006) and Josserand & Thoroddsen (2016) give excellent reviews of recent progress in the field and here we outline some of the early-stage phenomena that play important roles in the formation and evolution of a splash.

Before an impacting droplet touches down on a solid or liquid pool, the free surface of the droplet deforms due to the presence of the surrounding gas, see for example Wilson (1991), Smith *et al.* (2003), Mandre *et al.* (2009) and Mani *et al.* (2010). Several recent studies including Mandre & Brenner (2012), Kolinski *et al.* (2012), Kolinski *et al.* (2014) and de Ruiter *et al.* (2015) argue that the droplet begins to spread on an ultra-thin gas layer before it touches down, with Liu *et al.* (2015) showing that by draining the gas from under an impacting drop using a porous substrate, splashing can be inhibited. Recent progress on the early dynamics and advances in ultra-high speed imaging experiments have led to renewed insight into the motion inside the gas region under the impact and its consequences for touchdown (see Li & Thoroddsen (2015), Li *et al.* (2015), Langley *et al.* (2017) and Li *et al.* (2017)). Once touchdown has occurred, the gas layer retracts into a central gas bubble, which can have detrimental effects in, for example, printing applications, see amongst others Thoroddsen *et al.* (2005), Hicks & Purvis (2010) and Hicks & Purvis (2013).

For liquid-liquid impact problems in particular, the formation and evolution of the splash jets or ejecta are also of fundamental interest, with recent studies investigating the bending of the ejecta as it extends, which can lead to touchdown onto the bulk of the droplet or the solid/pool it is impinging upon, see for example Thoraval *et al.* (2012), Zhang *et al.* (2012*a*), Zhang *et al.* (2012*b*), Agbaglah *et al.* (2015) and Moore & Oliver (2018). After touching down, ligaments of fluid can be ‘sling-shot’ away from the drop, so that fluid is lost in the form of satellite droplets, see Thoroddsen *et al.* (2011). Furthermore, as the ejecta bends, vorticity can be shed from the highly-curved root of the jet, see Thoraval *et al.* (2012), Castrejón-Pita *et al.* (2012), Thoraval *et al.* (2013), Moore *et al.* (2014) and Agbaglah *et al.* (2015). It is an open question as to whether vorticity shedding causes the jet to bend or vice versa. If we wish to be able to control the amount of fluid lost to sling-shotting and the formation of satellite droplets in, say, inkjet printing as discussed in Martin *et al.* (2008), it is crucial to understand why the ejecta behaves as it does, which requires a thorough consideration of its early-time formation and growth. Thoroddsen (2002) first reported on experimental results in this challenging regime by considering the impact of drops onto thin liquid layers and describing the splash properties (contact radius, ejecta sheet velocity) for a wide range of viscosities obtained using different mixtures of water and glycerin that otherwise preserve properties such as density and viscosity. Soon after, Josserand & Zaleski (2003) proposed a theory predicting the transition between deposition and splashing, while deriving model expressions in the latter case for the jet root position, its velocity and the thickness of the outward-growing ejecta. Considering an almost equally rich interval of viscosities, it was concluded that this quantity plays a key role at the base of the jet in which vorticity is concentrated, with a viscous length scale becoming dominant in the analysis of the formation and thickening of the ejecta at early times. The splash mechanism is then further investigated and developed in the more recent work of Josserand *et al.* (2016).

In this study, we consider the collision of two droplets of the same Newtonian liquid. We perform a thorough qualitative and quantitative comparison of high-resolution numerical simulations performed in *Gerris* (Popinet (2003, 2009)) with the theoretical predictions of Wagner theory, named after the seminal work of Wagner (1932), for a range of droplet radii and velocities. For the purposes of this paper it is sufficient to remain in two-dimensions, although it is relatively straightforward to extend the analysis to axisymmetric or fully three-dimensional comparisons, with the natural increase in cost to computing power.

Wagner theory is an inviscid, incompressible, small-time asymptotic theory that is applicable to both liquid-solid and liquid-liquid impact problems, see for example Korobkin (1985), Armand & Cointe (1987) and Howison *et al.* (1991), while Howison *et al.* (2005) and Purvis & Smith (2005) in particular consider Wagner theory for liquid-liquid impact problems. Since Wagner theory was primarily developed to consider problems in naval architecture, it is particularly concerned with predictions of the force felt on an impacting solid, which compare favourably with numerical simulations and experiments, see for example Zhao & Faltinsen (1993) and Oliver (2007). On the other hand, since it contributes a lower-order effect to the force, the splash jet itself is less well-studied in the context of Wagner theory: in particular, several physical effects are neglected in the analysis (surface tension, the surrounding gas, gravity), which are likely to play a role in its evolution, see Moore & Oliver (2018).

Recent comparisons between Wagner theory, experiments and numerical simulations for droplets impacting onto a smooth solid substrate have been presented by Riboux & Gordillo (2014), Riboux & Gordillo (2015) (experiments) and Philippi *et al.* (2016) (simulations). These demonstrate a favourable comparison between the theory and the experiments/simulations for the size of the effective contact set (essentially, the speed of the root of the splash jet). In addition, Riboux & Gordillo (2014) and Riboux & Gordillo (2015) use Wagner theory to obtain the results of Oliver (2002) that give the thickness of the splash jet and its velocity at its root. They use these to solve a model for the evolution of the splash jet which couples the classical ballistic jet model of Wagner theory to a model for the growth of the jet tip, which give reasonable comparisons to their experimental data. Riboux & Gordillo (2017) have recently updated their approach to account for the effects of the boundary layer growing between the radial position of the stagnation point of the impact in the moving frame of reference and the root of the lamella, leading to improved agreement with experimental measurements.

Here we aim to extend this theory to a wide variety of liquid-liquid impact problems (see figure 1 for illustrative examples), while in addition comparing the theoretical prediction of the angle the jet root and the jet velocity to the numerical results. Our goal is twofold. Firstly, we wish to extend the range of impact problems to which Wagner theory gives a good approximation to include a wide class of liquid-liquid impacts. Secondly, we wish to show that the theory accurately predicts the position and velocity of the root of the jet. However, we shall demonstrate that Wagner theory cannot always predict the angle the jets are emitted at, which appears to be strongly affected by the build up of vorticity on the highly-curved free surfaces local to the jet roots and the ratio of the droplet radii. These conclusions allow us to isolate which properties we can reliably use Wagner theory to predict in models of splash jet evolution. Since impacts are such complex processes, with effects on various disparate lengthscales, having accurate boundary data for the jet at its root allows us to employ a simpler jet model with the impact itself modelled through appropriate boundary conditions, analogous to the model of Riboux & Gordillo (2015) for liquid-solid impact. In addition, further validation of the numerical code will support any future results for more complex scenarios that are not so

readily tackled using Wagner theory, for example the impact of two fluids with different densities, which has applications to aerosol formation in the dispersion of oil slicks or biological matter, see for example Murphy *et al.* (2015). Note that Semenov *et al.* (2015) exploit the similarity solution admitted by the geometry to investigate the impact of two fluid wedges of different densities numerically.

The structure of the paper is as follows. In §2, we shall outline the problem formulation and discuss the modelling assumptions necessary for the Wagner model. We present this model in §3, describing the asymptotic structure and the leading-order solution. In §4 we discuss the numerical configuration, leading to the computational results and comparison to the leading-order Wagner predictions in §5. Finally, we conclude with a summary of our findings and discuss avenues for future research in §6.

## 2. Problem formulation

We consider the two-dimensional vertical impact of two droplets of the same incompressible, Newtonian fluid. While there is an acknowledged influence of the gas layer between two droplets as they impact, we shall assume that the effect of any trapped central bubble on the later time motion is negligible in our leading-order analysis. Hence, in order to investigate the post-impact dynamics in detail, we shall seed the droplets so that at time  $t^* = 0^-$ , the droplets touch at the origin in the Euclidean  $(x^*, y^*)$ -plane; here and hereafter an asterisk indicates a dimensional variable. We shall check the veracity of this assumption later in §5. Gas – in most applications air, but we shall be general in this analysis – fills the region not occupied by the liquid.

The upper and lower droplets will be denoted by a + and a – respectively. Just before impact, the droplets are assumed to be moving uniformly with speeds  $V_{\pm}$ . The droplets are assumed to be circular, with their respective radii of curvature denoted by  $R_{\pm}$ . The liquids comprising the droplets and the gas have densities  $\rho_l, \rho_g$  and viscosities  $\mu_l, \mu_g$  respectively. The gas-liquid surface tension is denoted by  $\sigma$  and acceleration due to gravity is denoted by  $g$ . The configuration before impact is depicted in figure 1. We shall assume that  $R_- > R_+$  without loss of generality: since gravity will be negligible in this analysis, we could simply map  $y^* \mapsto -y^*$  to accommodate situations in which the lower droplet had a smaller radius of curvature. Note that, if  $R_- = \infty$ , the lower droplet is simply a deep pool, while if  $V_- = 0$ , the lower droplet is stationary.

After impact, at  $t^* = 0^+$ , the droplets collide and their free surfaces are violently disturbed, forming fast-moving, thin splash jets. The aim of this analysis is to predict the speed of the roots of these jets in the early stage of the motion, as well as the shape of the jet.

We denote variables in the liquid and the gas by  $l$  and  $g$  respectively. The Navier-Stokes equations are assumed to hold in each fluid, so that

$$\rho_i \left[ \frac{\partial \mathbf{u}_i^*}{\partial t^*} + (\mathbf{u}_i^* \cdot \nabla) \mathbf{u}_i^* \right] = -\nabla p_i^* + \mu \nabla^2 \mathbf{u}_i^*, \quad \nabla \cdot \mathbf{u}_i^* = 0, \quad (2.1)$$

for  $i = l, g$ , where  $\mathbf{u}_i^*$  is the velocity and  $p_i^*$  is the pressure in each fluid.

On the multivalued free surface of the liquid region, which we denote by  $y^* = h^*(x^*, t^*)$ , the kinematic condition is

$$v_n^* = \mathbf{u}_l^* \cdot \mathbf{n} \text{ on } y^* = h^*, \quad (2.2)$$

where  $\mathbf{n}$  is the outward pointing unit normal to the free surface and  $v_n^*$  is the normal speed of the boundary. Furthermore, we require there to be continuity of velocities and

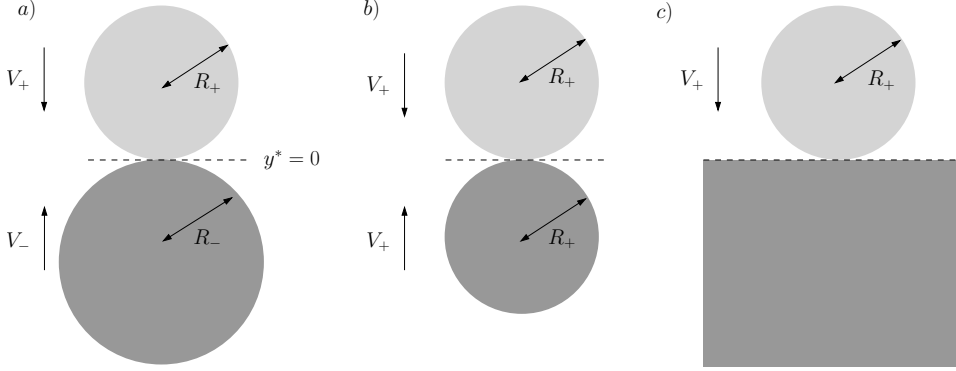


FIGURE 1. a) The general configuration of two circular droplets of the same liquid just before impact. The fluid in each droplet is coloured with different shades of grey for ease of viewing. The upper droplet is moving downwards with speed  $V_+$  and has a radius of curvature  $R_+$ . The lower droplet is moving upwards with speed  $V_-$  and has radius of curvature  $R_-$ . The droplets are surrounded by gas. b) The symmetric limit in which  $V_+ = V_-$  and  $R_+ = R_-$ , i.e.  $R = 1, V = 1$ . c) The deep pool limit in which  $V_- = 0, R_- = \infty$ , i.e.  $V = 0, R = \infty$ .

stress across the free surface, so that

$$\mathbf{u}_g^* = \mathbf{u}_l^*, \quad \mathbf{n} \cdot [\mathcal{T}_g - \mathcal{T}_l] = -\sigma \kappa \mathbf{n} \text{ on } y^* = h^*, \quad (2.3)$$

where  $\mathcal{T}_i$  denotes the Cauchy stress tensor in each fluid and  $\kappa = -\nabla \cdot \mathbf{n}$  is the curvature of the interface.

Initially, the droplet velocities dictate that

$$\mathbf{u}_l^*(x^*, y^*, 0) = \begin{cases} -V_+ \mathbf{j} & \text{for } y^* > 0, \\ V_- \mathbf{j} & \text{for } y^* < 0, \end{cases} \quad (2.4)$$

while the initial droplet shapes are given by

$$x^{*2} + (y^* \mp R_{\pm})^2 = R_{\pm}^2. \quad (2.5)$$

Finally, far from the impact, the gas velocity should decay, so that

$$\mathbf{u}_g^* \rightarrow \mathbf{0} \text{ as } x^{*2} + y^{*2} \rightarrow \infty. \quad (2.6)$$

### 2.1. Nondimensionalisation

We nondimensionalise distances by  $R_+$ , velocities by  $V_+$ , time by  $R_+/V_+$  and pressure by  $\rho_l V_+^2$ . The key dimensionless parameters are the Reynolds number in the liquid, the Weber number and the Froude number, defined by

$$\text{Re} = \frac{\rho_l R_+ V_+}{\mu_l}, \quad \text{We} = \frac{\rho_l R_+ V_+^2}{\sigma}, \quad \text{Fr}^2 = \frac{V_+^2}{g R_+}. \quad (2.7)$$

Moreover, the density, viscosity, radius of curvature and impact speed ratios are defined by

$$\rho = \frac{\rho_g}{\rho_l}, \quad \mu = \frac{\mu_g}{\mu_l}, \quad R = \frac{R_-}{R_+}, \quad V = \frac{V_-}{V_+}. \quad (2.8)$$

### 2.2. Modelling assumptions

For the purposes of our analysis in §3, we shall make the assumption that  $\text{Re}$ ,  $\text{We}$  and  $\text{Fr}^2$  are large, so that viscosity, surface tension and gravity are negligible, with the motion

dominated by inertia. For the impact of a water droplet with radius of curvature  $R_+ = 10^{-3}$  m at speed  $V_+ = 10$  ms $^{-1}$  with air as the surrounding gas, these numbers are

$$\text{Re} \approx 10^4, \text{ We} \approx 10^3, \text{ Fr}^2 \approx 10^2, \quad (2.9)$$

so that this assumption is not unreasonable at early time, at least in the bulk of the droplet. However, since the free surface is highly curved at the root of the splash jet, it may be that viscosity and surface tension are more relevant there, see for example Moore *et al.* (2014). We shall discuss this further in §5. We also note here that the viscosities we consider in this paper (for water) are in general at the lower limit of those considered in Thoroddsen (2002) and Josserand & Zaleski (2003). Moreover, for the example above, the typical timescale is  $R_+/V_+ \sim 10^{-4}$  s, which is significantly longer than the time scale  $t_v = 2R_+/(V_+\text{Re}) \sim 10^{-8}$  s, over which viscous effects dominate the flow at the root of the jet, discussed by Josserand & Zaleski (2003). Hence, we expect the inviscid regime to be appropriate.

In addition to these assumptions, since, in general, the gas-liquid viscosity and density ratios are small –  $\rho \approx 10^{-3}$ ,  $\mu \approx 10^{-2}$  for air-water systems – we shall also neglect the role of the gas layer post-impact in this analysis. Thus, for our analytical model, we will consider a one-fluid inviscid impact model known as the Wagner model.

### 3. Inviscid approximation: Wagner theory

As discussed in §2.2, in our theoretical model we neglect the effects of viscosity, surface tension, gravity and the surrounding gas. Since we neglect the gas in this section, we shall omit the subscript  $l$  on the liquid variables for convenience. At early times, say when  $t = \delta\hat{t}$  where  $0 < \delta \ll 1$ , the major effects of the impact are focussed close to the original contact point, where the two droplets are well-approximated by the parabola:

$$y = \frac{x^2}{2} - \delta\hat{t}, \quad y = -\frac{x^2}{2R} + \delta V\hat{t}. \quad (3.1)$$

The resulting early-time model is a variation of Wagner theory for solid-liquid impact, see for example Howison *et al.* (1991). The analysis we present here follows closely that of Purvis & Smith (2005), although we shall focus more on the jet root and the behaviour of the jet here.

At the outset, we note that, as in Purvis & Smith (2005), we shall include a vortex sheet (or interface) between the two droplets after impact, across which conditions of continuity of pressure and normal velocity are applied, see Saffman (1992). This is in contrast to Howison *et al.* (2005) who, in considering the impact of a liquid droplet onto a thin layer of the same fluid, state that for impacts initiating at a point, such a sheet can be ignored and the fluid treated as one body. To leading-order, this is true, since it transpires that the solutions with and without a vortex sheet are the same. However, proceeding to second-order, a local analysis at the jet root suggests that failing to include a vortex sheet leads to singularities in the local droplet free surface profiles that are inconsistent with Wagner theory. Thus, although a second-order analysis is well-beyond the scope of what we pursue here, we shall include a vortex sheet in our analysis for consistency and we denote it by  $y = \eta(x, t)$ . The subscripts  $\pm$  will be introduced to the flow variables in the upper and lower droplets respectively. Finally, we note that such a vortex sheet is, of course, only necessary in the context of a purely inviscid theory (which we pursue here), and will not be necessary when we consider numerical simulations of the full Navier-Stokes equations in §4 (although a passive tracer introduced to the simulations tracks the location of the initial interface between the droplets, see figure 8).

Under the above assumptions and since the flow is initially irrotational, there is a velocity potential  $\phi_{\pm}$ , such that  $\mathbf{u}_{\pm} = \nabla\phi_{\pm}$ . Thus, by the continuity condition,

$$\nabla^2\phi_{\pm} = 0 \text{ in the fluid,} \quad (3.2)$$

with the liquid pressure given by Bernoulli's equation

$$\frac{1}{\delta} \frac{\partial\phi_{\pm}}{\partial\hat{t}} + p_{\pm} + \frac{1}{2} |\nabla\phi_{\pm}|^2 = \frac{1}{2}, \quad (3.3)$$

where the Bernoulli constant has been chosen by considering the far-field behaviour of the flow in the upper droplet.

On the free surfaces, which we denote by  $h_+$  and  $h_-$  for the upper and lower droplets respectively, the kinematic and dynamic conditions are given by

$$\frac{\partial\phi_{\pm}}{\partial y} = \frac{1}{\delta} \frac{\partial h_{\pm}}{\partial\hat{t}} + \frac{\partial\phi_{\pm}}{\partial x} \frac{\partial h_{\pm}}{\partial x}, \quad p_{\pm} = 0 \text{ on } y = h_{\pm}. \quad (3.4)$$

Across the vortex sheet, we enforce

$$\frac{\partial\phi_{\pm}}{\partial y} = \frac{1}{\delta} \frac{\partial\eta}{\partial\hat{t}} + \frac{\partial\phi_{\pm}}{\partial x} \frac{\partial h_{\pm}}{\partial x}, \quad p_+ = p_- \text{ on } y = \eta. \quad (3.5)$$

Far from the impact, the flow velocities are given by the impact velocities, so that

$$\nabla\phi_+ \rightarrow -\mathbf{j} \text{ as } x^2 + y^2 \rightarrow \infty, y > 0, \quad \nabla\phi_- \rightarrow V\mathbf{j} \text{ as } x^2 + y^2 \rightarrow \infty, y < 0, \quad (3.6)$$

while the free surfaces must approach the parabolic profiles (3.1) so that

$$h_+ \sim \frac{x^2}{2} - \delta\hat{t}, \quad h_- \sim -\frac{x^2}{2R} + \delta V\hat{t}, \text{ as } |x| \rightarrow \infty. \quad (3.7)$$

Finally, the initial conditions are given by

$$\phi_+(x, y, 0) = -y, \quad \phi_-(x, y, 0) = Vy, \quad h_+(x, 0) = \frac{x^2}{2}, \quad h_-(x, 0) = -\frac{x^2}{2R}. \quad (3.8)$$

Note that (3.6) implies that  $\phi_+ \sim -y + F(\hat{t})$  and  $\phi_- \sim Vy + G(\hat{t})$  in the far-field of the fluids. We are able to determine  $F(\hat{t})$  and  $G(\hat{t})$  by matching to an 'outer-outer' region where  $x, y$  are  $O(1)$ , which we discuss in Appendix A. In this region, the droplets are undeformed to leading order, with the perturbation to the vertical impact velocities driven by the dipole at the origin. Note that this perturbation is only important in the outer region discussed in §3.2 at second order, which we do not consider here, and for the purposes of the rest of this paper, it suffices to say here that  $F$  and  $G$  are  $O(\delta)$  and thus

$$\phi_+ \rightarrow -y + O(\delta) \text{ as } x^2 + y^2 \rightarrow \infty, y > 0, \quad \phi_- \rightarrow Vy + O(\delta) \text{ as } x^2 + y^2 \rightarrow \infty, y < 0, \quad (3.9)$$

### 3.1. Asymptotic structure

The impact breaks down into three distinct regimes based on the timescale  $\delta$ , which are depicted in figure 2. In the outer region, where lengths scale with  $\delta^{1/2}$ , the thin jet can be neglected and the free surface and interface boundary conditions linearise on to the undisturbed waterline, leading to a mixed boundary value problem. Local to the jet roots, the outer velocity and pressure are singular, which is rectified by matching to an inner region of size  $O(\delta^{3/2})$  centred around the root, that is two orders of magnitude smaller than the outer region. In the inner region, the free surface turns over into the

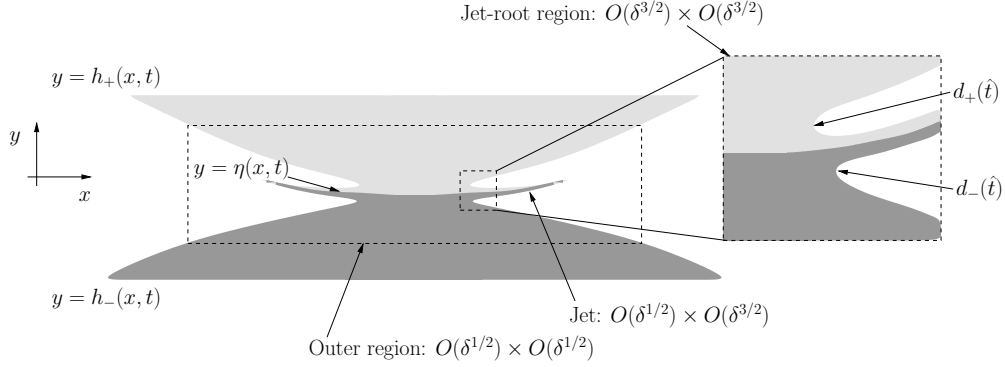


FIGURE 2. The Wagner asymptotic structure based on the small timescale  $\delta$ . The fluid in each droplet is coloured with different shades of grey for ease of viewing. The horizontal coordinates of the upper and lower turnover points are denoted by  $\pm d_{\pm}(\hat{t})$  respectively. Note that the problem is symmetric about the  $y$ -axis.

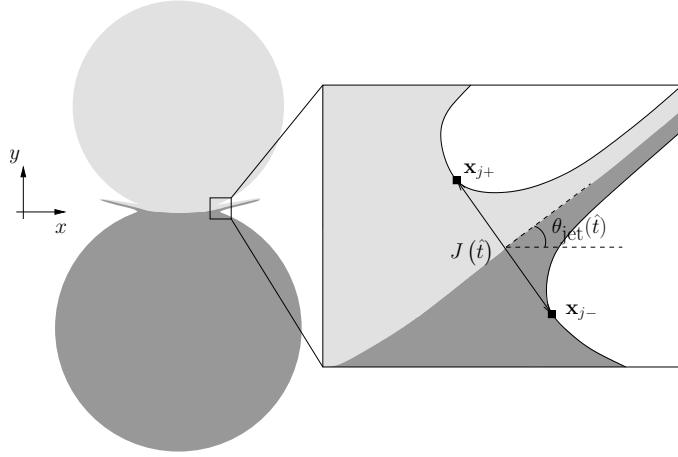


FIGURE 3. A close-up of the right-hand jet root to highlight the main quantities of interest local to the turnover region. The fluid in each droplet is coloured with different shades of grey for ease of viewing. The turnover points  $\mathbf{x}_{j\pm}$  as defined in (3.10) are taken to be the points at which the curvature of the free surface is locally maximised. The thickness of the jet is taken to be the distance between the turnover points and is denoted by  $J(\hat{t})$ . The angle  $\theta_{\text{jet}}(\hat{t})$  is a measure of the local angle the jet makes to the horizontal. Specifically, we take  $\theta_{\text{jet}}(\hat{t})$  to be the angle formed when we take the local tangent to the interface between the fluids at the point at which the line joining the turnover points intersects the interface.

splash jet. The final regions are the thin, fast-moving jets, whose lengths are comparable to the outer region and whose thicknesses are comparable to the inner.

Since some of the key results that we aim to extract from the model and compare with our numerical simulations are the location of the jet roots, the thickness of the jet at its root and the angle the jet makes to the horizontal, we briefly clarify what we mean by these quantities here. Without loss of generality we shall describe these properties for the right-hand jet. The upper and lower jet root coordinates are taken to be  $\mathbf{x}_{j\pm} = (d_{\pm}(\hat{t}), h_{\pm}(d_{\pm}(\hat{t}), \hat{t}))$ , and, as seen in figure 3, these are taken to be the points at which the curvature of the free surfaces are maximised locally. Note that this requires the jet to have formed: when the jet initially emerges, this criterion is not necessarily a sensible definition, particularly with the presence of a tip, but recall that



we are not considering the initial emergence of the jet in our analysis. Furthermore, this definition may also break down in the event that the free surface becomes unstable to small perturbations (perhaps driven by viscosity or surface tension forces) local to the jet root. In this purely inviscid theory, we do not see such instabilities, but it is something that must be considered later in the numerical study. As seen in §5.1, however, over the timescales we consider and with the fluids we study, we do not see such issues in this analysis. We shall refer to these upper and lower jet locations as the *turnover points* of the droplet free surfaces throughout our analysis. In summary, for the whole impact, there are four turnover points, two for each of the jets with the right-hand turnover points located at  $\mathbf{x}_{j\pm}^*$ , where

$$\mathbf{x}_{j\pm}^* = R_+ \mathbf{x}_{j\pm} = R_+ (d_{\pm}(\hat{t}), h_{\pm}(d_{\pm}(\hat{t}), \hat{t})), \quad (3.10)$$

using the notation of figure 3. The left-hand turnover points are easily deduced from the symmetry of the problem.

Integral to the inviscid theory is that the distance between the turnover points (scaled by  $R_+$ ), defined by the thickness  $J(\hat{t})$  in figure 3, is of  $O(\delta^{3/2})$ . We note that this is an order of magnitude smaller than the  $O(\delta)$  stated in Josserand & Zaleski (2003) for an inviscid approximation of the local jet thickness, but it is well-established in Wagner theory – see for example, Howison *et al.* (1991) – that the only consistent asymptotic structure for a purely inviscid model requires the local jet thickness at its root to be two orders of magnitude smaller than the size of the outer region, which is of  $O(\delta^{1/2})$ , as stated above. The veracity of the above assumption is realised by both the consistency of the matched asymptotic solution and the excellent comparisons between the predictions of the location of the turnover points and the numerical results in §5.

Finally, we need to define an angle  $\theta_{\text{jet}}(\hat{t})$  that gives a representation of the angle the jet makes to the horizontal. The choice of such an angle is not unique. In this paper, we instantaneously draw a straight line between the upper and lower turnover points, this line intersects the interface between the fluids. The *jet angle*,  $\theta_{\text{jet}}(\hat{t})$ , is taken to be the angle made by the local tangent to the interface to the horizontal at this point. Other definitions of the jet angle have also been postulated, for example the angle between the normal to the line drawn between  $\mathbf{x}_{j\pm}^*$  and the horizontal (as used in, for example, Thoraval *et al.* (2012)), or the angle made to the horizontal by a line drawn from the jet root to the jet tip (which does not take into account jet bending due to the surrounding air, see Moore & Oliver (2018) for example). We do not seek to discuss the relative merits of one definition over another here, but state that we have chosen our definition of the jet angle to tie most closely to the inviscid analysis we pursue in the following sections. At the outset, we state that this is the quantity that is most poorly predicted by the inviscid theory, and it appears that viscosity and surface tension may have crucial roles in its evolution.

### 3.2. Outer region

In the outer region, we scale

$$(x, y) = \delta^{1/2}(\hat{x}, \hat{y}), \quad \phi_{\pm} = \delta^{1/2}\hat{\phi}_{\pm}, \quad p_{\pm} = \delta^{-1/2}\hat{p}_{\pm}, \quad h_{\pm} = \delta\hat{h}_{\pm}, \quad \eta = \delta\hat{\eta}, \quad d_{\pm} = \delta^{1/2}\hat{d}_{\pm}, \quad (3.11)$$

and expand the variables in asymptotic series in powers of delta, viz:

$$\hat{\phi}_{\pm} = \hat{\phi}_{\pm 0} + \delta^{1/2}\hat{\phi}_{\pm 1} + O(\delta) \quad (3.12)$$

etc. For notational convenience – and subject to the assumption mentioned above – we shall denote the leading-order term in the expansions of  $\hat{d}_{\pm}$  by  $\hat{d}_0$ .

$$\begin{array}{c}
\nabla^2 \hat{\phi}_{+0} = 0 \\
\hat{\phi}_{+0} = 0, \quad \frac{\partial \hat{\phi}_{+0}}{\partial \hat{y}} = \frac{\partial \hat{h}_{+0}}{\partial \hat{t}} \quad \hat{\phi}_{+0} = \hat{\phi}_{-0}, \quad \frac{\partial \hat{\phi}_{\pm 0}}{\partial \hat{y}} = \frac{\partial \hat{\eta}_0}{\partial \hat{t}} \quad \hat{\phi}_{+0} = 0, \quad \frac{\partial \hat{\phi}_{+0}}{\partial \hat{y}} = \frac{\partial \hat{h}_{+0}}{\partial \hat{t}} \\
\hat{\phi}_{-0} = 0, \quad \frac{\partial \hat{\phi}_{-0}}{\partial \hat{y}} = \frac{\partial \hat{h}_{-0}}{\partial \hat{t}} \quad -\hat{d}_0(\hat{t}) \quad \hat{d}_0(\hat{t}) \quad \hat{\phi}_{-0} = 0, \quad \frac{\partial \hat{\phi}_{-0}}{\partial \hat{y}} = \frac{\partial \hat{h}_{-0}}{\partial \hat{t}} \\
\nabla^2 \hat{\phi}_{-0} = 0
\end{array}$$

FIGURE 4. The leading-order outer problem for the velocity potentials  $\hat{\phi}_{\pm 0}$ . We have integrated the dynamic boundary conditions with respect to time and applied the leading-order initial condition to obtain the boundary conditions  $\hat{\phi}_{\pm 0} = 0$  on the free surfaces and  $\hat{\phi}_{+0} = \hat{\phi}_{-0}$  on the interface. The problem is supplemented by the far-field conditions that  $\hat{\phi}_{+0} \sim -\hat{y}$  as  $\hat{x}^2 + \hat{y}^2 \rightarrow \infty$  and  $\hat{\phi}_{-0} \sim V\hat{y}$  as  $\hat{x}^2 + \hat{y}^2 \rightarrow \infty$ . The free surfaces have initial profiles given by  $\hat{h}_{+0} = \hat{x}^2/2$  and  $\hat{h}_{-0} = -\hat{x}^2/(2R)$  respectively. This problem is co-dimension two in the sense that  $d_0(\hat{t})$  must be solved for as part of the problem.

The leading-order problem is depicted in figure 4. It is a Riemann-Hilbert boundary value problem of index  $-1$ , since  $-$  as is confirmed when considering the inner region – the velocity potentials have square-root behaviour close to the turnover points,  $\pm \hat{d}_0(\hat{t})$ . The solution for the complex velocities  $\hat{w}_{\pm 0} = \hat{\phi}_{\pm 0} + i\hat{\psi}_{\pm 0}$  can readily be found in terms of the complex variable  $\hat{z} = \hat{x} + i\hat{y}$ :

$$\hat{w}_{\pm 0}(\hat{z}, \hat{t}) = i \left[ \left( \frac{1-V}{2} \right) \hat{z} + \left( \frac{1+V}{2} \right) \sqrt{\hat{z}^2 - \hat{d}_0(\hat{t})^2} \right], \quad (3.13)$$

where the branch cut for the square root is taken along the real axis for  $|\hat{x}| > \hat{d}_0$ . Evaluating (3.13) on the real axis and integrating allows us to determine the leading-order upper and lower free surface profiles, which take the form

$$\hat{h}_{+0} = \frac{\hat{x}^2}{2} - \left( \frac{1-V}{2} \right) \hat{t} - \left( \frac{1+V}{2} \right) \int_0^{\hat{t}} \frac{|\hat{x}|}{\sqrt{\hat{x}^2 - \hat{d}_0(s)^2}} ds, \quad (3.14)$$

$$\hat{h}_{-0} = -\frac{\hat{x}^2}{2R} - \left( \frac{1-V}{2} \right) \hat{t} + \left( \frac{1+V}{2} \right) \int_0^{\hat{t}} \frac{|\hat{x}|}{\sqrt{\hat{x}^2 - \hat{d}_0(s)^2}} ds. \quad (3.15)$$

In order to complete the leading-order solution, we require a condition for the leading-order turnover point location,  $\hat{d}_0$ . For this we use the *Wagner condition*, which is a matching condition with the inner region, but in essence says that in the outer region, the leading-order free surfaces and the vortex sheet must coincide at the turnover point, so that

$$\hat{h}_{+0}(\hat{d}_0(\hat{t}), \hat{t}) = \hat{h}_{-0}(\hat{d}_0(\hat{t}), \hat{t}) = \eta_0(\hat{d}_0(\hat{t}), \hat{t}). \quad (3.16)$$

Upon substituting (3.14)–(3.15) into (3.16), we obtain an integral equation that may be inverted subject to the initial condition that  $\hat{d}_0(0) = 0$ , giving

$$\hat{d}_0(\hat{t}) = 2\sqrt{\frac{(1+V)R}{1+R}} \hat{t}. \quad (3.17)$$

Note that in the symmetric regime where  $R, V = 1$  this reproduces the well-known formula for the turnover point location for the impact of a parabola onto a solid,  $\hat{d}_0 = 2\sqrt{\hat{t}}$ , see for example Korobkin (2007). The free surface height at the turnover point is therefore

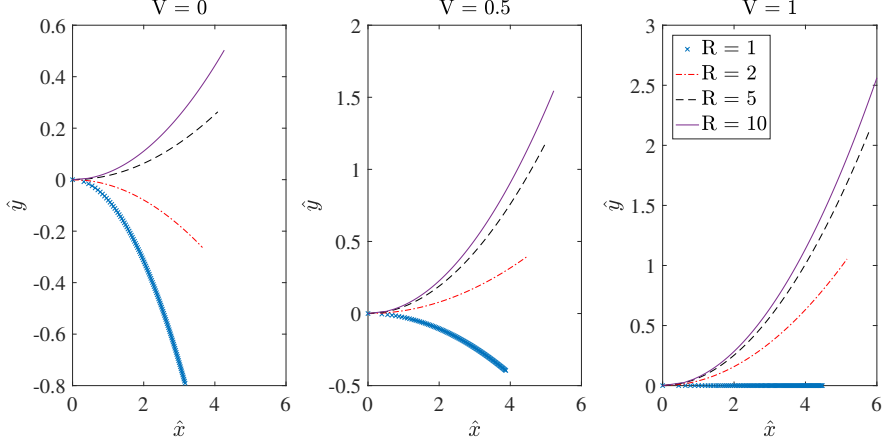


FIGURE 5. The leading-order jet-root curve for  $\delta = 0.1$  and various values of  $R$  and  $V$ . Note that  $V = 0$  corresponds to a stationary lower droplet and  $V = 1$  to symmetric impact speeds, while  $1/R = 1$  represents identical droplets and  $1/R \rightarrow 0$  allows the lower droplet to approach a half-space.

given by

$$\hat{h}_{+0}(\hat{d}_0(\hat{t}), \hat{t}) = \frac{(3RV + R - V - 3)}{2(1 + R)} \hat{t}. \quad (3.18)$$

Finally, after evaluating (3.13) for  $|\hat{x}| < \hat{d}_0$  and carefully integrating with respect to time, we are able to determine the leading-order vortex sheet location:

$$\hat{\eta}_0 = \frac{\hat{x}^2}{2} - \left(\frac{1-V}{2}\right) \hat{t} - \left(\frac{1+V}{2}\right) |\hat{x}| \int_0^{\hat{\omega}_0} \frac{1}{\sqrt{\hat{x}^2 - \hat{d}_0(s)^2}} ds, \quad (3.19)$$

where we have used the Wagner condition (3.16) and where  $\hat{t} = \hat{\omega}_0(\hat{x})$  is the location of the turnover curve – i.e.  $\hat{\omega}_0 = \hat{d}_0^{-1}$ , provided that the inversion is well-defined. As discussed in Howison *et al.* (1991), inversion is possible provided that  $\dot{\hat{d}}_0(\hat{t}) > 0$ .

Therefore recalling (3.10), and that to leading-order  $\mathbf{x}_{j+} = \mathbf{x}_{j-} = \mathbf{x}_j$ , we have

$$\mathbf{x}_j = \left( \delta^{1/2} \hat{d}_0(\hat{t}), \delta \hat{h}_{+0}(\hat{d}_0(\hat{t}), \hat{t}) \right), \quad (3.20)$$

where  $\hat{d}_0(\hat{t})$  and  $\hat{h}_{+0}(\hat{d}_0(\hat{t}), \hat{t})$  are given by (3.17)–(3.18). Hence, after returning to dimensional variables, to leading order the right-hand jet root moves along the curve

$$\mathbf{x}_j^* = (x_j^*, y_j^*) = \left( 2\sqrt{\frac{(1+V)R}{1+R}} \sqrt{R_+ V_+ t^*}, \left( \frac{3RV + R - V - 3}{2(1+R)} \right) V_+ t^* \right). \quad (3.21)$$

We shall henceforth refer to this as the ‘jet-root curve’.

We plot curves of the locus mapped out by the jet root region for various values of  $R$  and  $V$  in figure 5. It is clear that the shape of the jet-root curve depends strongly on  $R$  and  $V$ . In particular, in figure 5a, when the lower droplet is stationary, the jet root location moves towards the lower droplet when the radii of curvature are similar, but curves away from the lower droplet as it approaches a half-space. There is similar behaviour as we increase the velocity of the lower droplet, although the transition from a downward-moving to an upward-moving jet root happens earlier, as seen in figure 5b. In figure 5c, the impact speeds are identical, so that for  $R = 1$  we see that  $y_j = 0$  to

leading order, as expected. However, note that even for  $R, V \neq 1$  we can get  $y_j = 0$  to leading order provided the numerator for the  $\hat{y}$ -coordinate in (3.21) is zero, that is, when

$$V = \frac{R-3}{1-3R}. \quad (3.22)$$

Finally, we note that after substituting for  $\hat{d}_0$  into (3.19), the vortex sheet location is found to be

$$\hat{\eta}_0 = \left( \frac{R-1}{4R} \right) \hat{x}^2 - \left( \frac{1-V}{2} \right) \hat{t}. \quad (3.23)$$

This is simply the average location of the undisturbed parabolae (3.1); as expected the vortex sheet moves with the flow, see Saffman (1992). Moreover, since the tangential velocity is continuous across  $\hat{\eta}$  to leading-order, the vortex sheet is completely passive in the leading-order theory.

### 3.3. Inner region

Local to the jet root (3.21), the droplet free surfaces turn over in a region that is two orders of magnitude smaller than the outer region. This displacement of the free surface forms a fast-moving, thin jet of fluid. In this section, we shall report the existing results in the literature that allow us to determine the thickness and velocity of the jets at their roots, which we can then compare to the full numerical simulations we perform in §5. By symmetry, we need only consider the right-hand jet root here.

Before starting, we note it is natural that the jet root region should be aligned with the slope of the vortex sheet at  $x^* = d^*(t^*)$ , which can be calculated from (3.23) to be at an angle

$$\alpha = \delta^{1/2} \left( (R-1) \sqrt{\frac{1+V}{R(1+R)}} \right) \sqrt{\hat{t}} + o(\delta^{1/2}) \quad (3.24)$$

to the horizontal. However, since  $\alpha$  is small and we shall only pursue a leading-order solution in this paper, we shall neglect any rotation of the jet root region in our analysis, since it will make the analysis significantly more complex while having no impact on the leading-order results. We shall, however, return in §5 to discuss the angle (3.24) and how it compares to the angle  $\theta_{\text{jet}}$  as defined in figure 3.

The appropriate scales for this region are derived in Howison *et al.* (1991) for the related problem of water entry — in particular, their *deadrise angle*  $\varepsilon$  is equivalent to  $\delta^{1/2}$  here — and they are given by

$$x = \delta^{1/2} \hat{d}_+(\hat{t}) + \delta^{3/2} X, \quad y = \delta \hat{h}_{+0}(\hat{d}_0(\hat{t}), \hat{t}) + \delta^{3/2} Y, \quad (3.25)$$

with the velocity potential and pressure in each fluid scaled by

$$\phi_{\pm} = \delta \left( \hat{d}_+(\hat{t}) X + \Phi_{\pm} \right), \quad p_{\pm} = \delta^{-1} P_{\pm}. \quad (3.26)$$

In the inner region, the free surfaces are denoted by  $Y = H_{\pm}$  and the vortex sheet is denoted by  $Y = \Delta$ , where

$$h_{\pm} = \delta \hat{h}_{+0}(\hat{d}_0(\hat{t}), \hat{t}) + \delta^{3/2} H_{\pm}, \quad \eta = \delta \hat{h}_{+0}(\hat{d}_0(\hat{t}), \hat{t}) + \delta^{3/2} \Delta. \quad (3.27)$$

Upon expanding the rescaled equations in asymptotic series of the form  $\Phi_{\pm} = \Phi_{\pm 0} + o(1)$  etc., the leading-order problem is quasi-steady and is depicted in figure 6. There is a stagnation point on the vortex sheet where dividing streamlines in the upper and lower droplets meet. Fluid to the left of the dividing streamlines heads back into the bulk of the droplets, while fluid to the right of the dividing streamlines is forced into the jet. The

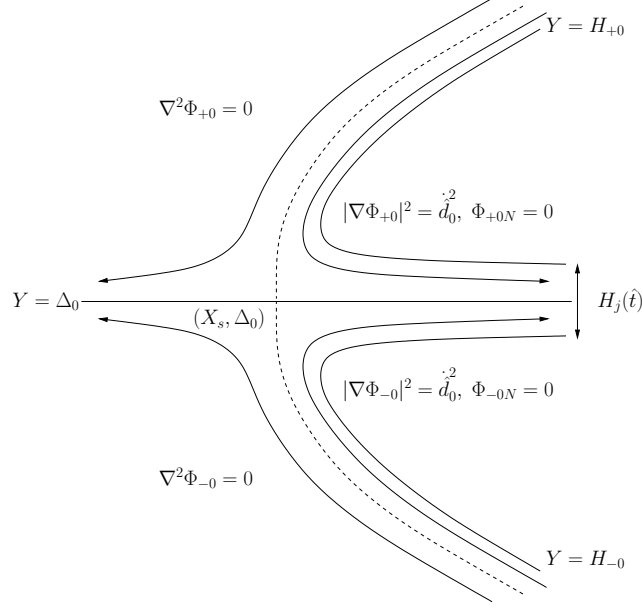


FIGURE 6. The leading-order-inner problem for the velocity potentials,  $\Phi_{\pm 0}$ , upper and lower free surfaces  $H_{\pm 0}$  and vortex sheet  $\Delta_0$ . Dividing streamlines in each fluid are denoted by the dashed lines. They meet on the vortex sheet at a stagnation point. The far-field jet thickness is denoted by  $H_j(\hat{t})$ .

quantity  $H_j(\hat{t})$  denotes the leading order *downstream* thickness of the jet in the inner region (as opposed to  $J(\hat{t})$ , which is measured at the jet root, see figure 3).

Since the vortex sheet essentially plays a passive role in the leading-order-outer problem, we are able to deduce that the leading-order-inner problem must be symmetric about the sheet, which is thus simply given by  $\Delta_0(X, \hat{t}) = 0$  at leading-order. We would need to proceed to second-order in the outer problem to show this rigorously, but we omit the analysis here for brevity. We can use the symmetry and the complex variable  $Z = X + iY$  to derive the parametric solution for the leading-order complex potentials  $W_{\pm 0} = \Phi_{\pm 0} + i\Psi_{\pm 0}$  as given in Oliver (2002):

$$W_{\pm 0} = C_{\pm}(\hat{t}) + \frac{\hat{d}_0 H_j}{2\pi} (\zeta - \log \zeta), \quad Z = -\frac{H_j}{2\pi} \left( 1 + \zeta + 4\sqrt{\zeta} + \log \zeta \right), \quad (3.28)$$

where the branch cuts are taken along  $\text{Re}(\zeta) < 0$ ,  $\text{Im}(\zeta) = 0$  with  $H_{\pm 0}$  corresponding to  $\text{Re}(\zeta) < 0$ ,  $\text{Im}(\zeta) = \mp 0$  respectively.

Matching with the leading-order outer solution as in Oliver (2002) gives the leading-order jet thickness to be

$$H_j(\hat{t}) = \frac{\pi}{16} \frac{(1+V)^2 \hat{d}_0(\hat{t})}{\hat{d}_0(\hat{t})^2} = \frac{\pi(1+V)^{3/2}}{8} \sqrt{\frac{1+R}{R}} \hat{t}^{3/2}, \quad (3.29)$$

with the far-field jet velocity,  $U_j(\hat{t})$ , given by

$$U_j = 2\hat{d}_0 = 2\sqrt{\frac{(1+V)R}{1+R}} \hat{t}^{-1/2}, \quad (3.30)$$

where the factor of two occurs due to the velocity of the moving frame.

Although we omit this here for brevity, by proceeding to second-order in the outer

region it is possible to show that the  $O(\delta)$ -correction to the horizontal turnover point locations  $d_1 = 0$ , as in solid-liquid parabola impacts, see Korobkin (2007) and Oliver (2007). In order to calculate the  $O(\delta^{3/2})$ -corrections to the horizontal jet-root coordinates,  $d_{\pm 2}$ , we would need to proceed to second order in the inner region as well, which is a non-straightforward task, particularly as the rotation of the inner region will be important at this order. Unfortunately, without  $d_{\pm 2}$  we are unable to get an exact leading-order form for  $J(\hat{t})$ , although it is clear that  $J(\hat{t}) \propto \hat{t}^{3/2}$ : in particular, the vertical distance between the turnover points in the rotated frame is given by  $(1 + 4/\pi)H_j(t) \propto \hat{t}^{3/2}$ , as can be deduced by evaluating (3.28) on  $\xi < 0, \eta = \pm 0$  and finding the turnover points. We shall discuss the thickness at the jet root in more detail in §5.2.

Thus, in summary, the right-hand jet root is located at  $\mathbf{x}_j^*$  given by (3.21) and is aligned at a small angle to the horizontal, (3.24). In the inner region local to  $\mathbf{x}_j^*$ , the free surfaces turn over and fluid is ejected into a jet with leading-order velocity  $\delta^{-1/2}V_+U_j$ , with the leading-order jet thickness given by  $\delta^{3/2}R_+H_j$  as we approach the jet root from downstream in the jet.

### 3.4. Jet region

The information we have obtained from the leading-order-outer and leading-order-inner regions indicates that the fast-moving jet is emitted almost horizontally from the jet root as it moves along the curve (3.21). Since the jet has a long, thin aspect ratio, we can still derive a model for the leading-order jet thickness and leading-order horizontal component of velocity using the standard Wagner jet scalings discussed in Howison *et al.* (1991). The angle at which the jet is emitted affects the centreline of the jet, not its thickness, so, assuming that the jet centreline does not deviate significantly from the curve (3.21) we can neglect the angle here. Such an assumption seems reasonable in the early stages of impact, particularly in the absence of air effects, and we shall discuss its validity in §5.4. Determining the centreline of the jet is an interesting problem in its own right, see Moore & Oliver (2018), but not one we seek to analyse here.

In order to study the jet evolution it is sensible to move to a frame  $(s, n)$  based on the curve (3.21), where we shall use  $s$  to represent arc length along the curve and  $n$  is in the normal direction to the curve. The curvature is denoted by  $\kappa(s)$ . Based on (3.21) and the known size of the jet root, we scale

$$s = \delta^{1/2}\bar{s}, \quad n = \delta^{3/2}\bar{n}. \quad (3.31)$$

It is straightforward to show that  $\kappa = O(1)$ , so that the radius of curvature of the curve (3.21) is much larger than the length of the jet<sup>†</sup>. Moreover, by the symmetry at leading-order in the jet root, we can neglect the interface in the jet and simply treat the jet as a single fluid. Hence, introducing the leading-order tangential component of jet velocity  $\bar{u}_0$  (scaled by  $\delta^{-1/2}$ ) and the leading-order jet thickness  $\bar{\chi}_0$  (scaled by  $\delta^{3/2}$ ), we can derive, akin to the jet in solid-liquid impact, the zero-gravity shallow water equations in  $\bar{s} > \hat{d}_0(\hat{t})$ :

$$\bar{u}_{0\hat{t}} + \bar{u}_0\bar{u}_{0\bar{s}} = 0, \quad \bar{\chi}_{0\hat{t}} + (\bar{u}_0\bar{\chi}_0)_{\bar{s}} = 0, \quad (3.32)$$

subject to the jet root conditions

$$\bar{u}_0(\hat{d}_0(\hat{t}), \hat{t}) = U_j(\hat{t}), \quad \bar{\chi}_0(\hat{d}_0(\hat{t}), \hat{t}) = H_j(\hat{t}). \quad (3.33)$$

<sup>†</sup> Essentially meaning we can replace  $(\bar{s}, \bar{n})$  by  $(\hat{x}, \delta\hat{y})$ .

Using the method of characteristics, we can solve (3.32)–(3.33) to find that

$$\bar{u}_0 = \frac{\bar{s}}{\hat{t}}, \quad \bar{\chi}_0 = \frac{4\pi(1+V)^4 R^2 \hat{t}^4}{(1+R)^2 \bar{s}^5}. \quad (3.34)$$

Therefore, since  $\bar{\chi}_0 > 0$  for all  $\bar{\xi} > \hat{d}_0(\hat{t})$ , the jet is predicted to be infinitely long and to achieve this in an infinitesimally small amount of time (note that  $\bar{u}_0(\hat{d}_0(\hat{t}), \hat{t}) \sim \hat{t}^{-1/2}$  as  $\hat{t} \rightarrow 0$ ). This is a well-known drawback of the Wagner jet model, with further physical effects likely to play a key role further down the jet. This problem is discussed in more detail for liquid-solid impacts after the jet has detached in Riboux & Gordillo (2015), where the Wagner jet model given by (3.32)–(3.33) is coupled to a model for the evolution of the tip (in their paper the lamella *rim*), which incorporates the role of surface tension and the surrounding gas. Note that in such a model, the location of the jet centreline is important, see Moore & Oliver (2018), and this would require a more careful analysis of the second-order-outer and second-order-inner problems in the Wagner structure, as discussed in §3.3.

#### 4. Numerical configuration

We use the open-source package *Gerris* (Popinet (2003, 2009)) to validate the previous analytical findings and complement the investigation with flow information from both within and outside of the discussed asymptotic framework. The freely available software has enjoyed tremendous success in the multiphase flow community for almost a decade and a half in a variety of contexts ranging from microfluidics to geophysical flows. Of particular relevance to the present discussion is the well-suited environment for the study of drop impact, which requires careful consideration of a large range of scales, as well as possible topological changes. Especially during the last five years, also aided by advances in experimental/imaging equipment, a range of influential studies using *Gerris* as computational support have been published. These are concerned with impacts of liquid drops onto both solid surfaces (Visser *et al.* (2015); Philippi *et al.* (2016); Wildeman *et al.* (2016); Jian *et al.* (2018)) and liquid pools (Thoraval *et al.* (2012); Agbaglah *et al.* (2015)). The scope of the work is of both fundamental interest and practical significance, given the translation of the results into engineering contexts related to inkjet printing, agricultural sprays, combustion and environmental research. The underlying algorithms have also been proven sufficiently robust even in challenging high speed regimes of relevance to the aircraft industry, as elaborated on in the recent study of Cimpeanu & Papageorgiou (2018).

To aid our discussion of the direct numerical simulation setup, we refer to figure 7 below. Where suitable, the notation from previous sections is preserved, with  $(\cdot)_g$  and  $(\cdot)_l$  denoting quantities in gas and liquid respectively, while subscripts  $(\cdot)_-$  and  $(\cdot)_+$  will be used to indicate the bottom and top droplets. For all of our simulations we shall take the gas to be air and the liquid to be water at room temperature, and therefore, the appropriate physical parameters are as follows: densities  $\rho_l = 999.98 \text{ kg/m}^3$  and  $\rho_g = 1.21 \text{ kg/m}^3$ ; viscosities  $\mu_l = 10^{-3} \text{ kg/m}\cdot\text{s}$  and  $\mu_g = 1.81 \cdot 10^{-5} \text{ kg/m}\cdot\text{s}$ ; and surface tension coefficient  $\sigma = 0.072 \text{ kg/s}^2$ . The radius of the top droplet is considered to be the reference lengthscale in the domain, with  $R_+ = 10^{-3} \text{ m}$  selected as being representative. Its reference impact velocity has a magnitude of  $V_+ = 10 \text{ m/s}$ , giving rise to the following dimensionless parameter setup

$$\text{Re} = 9999.8 \approx 10^4, \quad \text{We} = 1388.86 \approx 10^3, \quad \text{Fr}^2 = 100.96 \approx 10^2, \quad (4.1)$$

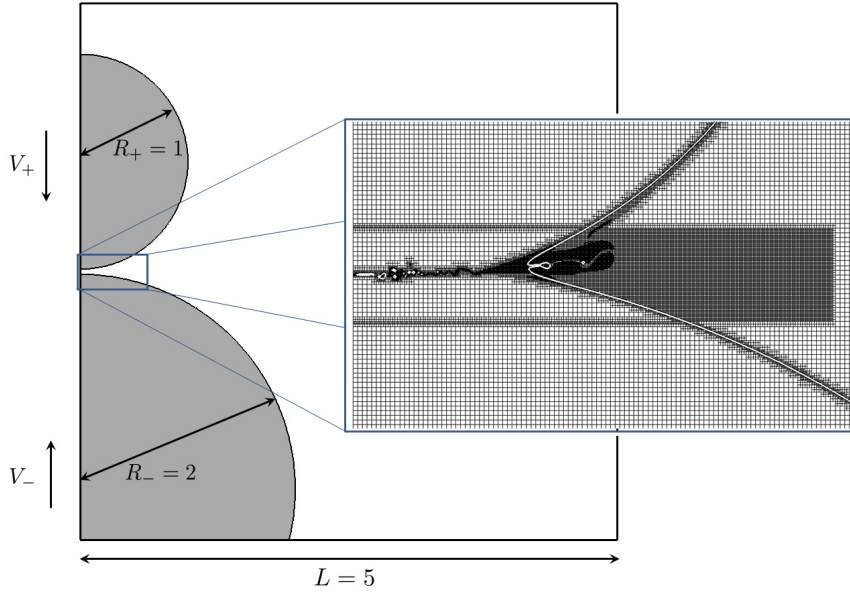


FIGURE 7. Direct numerical simulation setup, with the background image illustrating the finite computational domain at  $t = 0$  for a test case described by  $R = 2$  and  $V = 1$ . The inset focuses on details of the grid refinement at later times ( $t = 0.05$ , once impact has taken place and the jet is formed), when temporal and spatial adaptive criteria based on changes in velocity, vorticity and interfacial location are imposed.

all sufficiently large to be in line with the range of the validity of the model discussed in §3. We do emphasise, however, that some assumptions considered in the analytical work are not reflected in the numerical setup: gravity, the liquid viscosity, surface tension and the surrounding gas are present in direct numerical simulations. These additional effects aim to bring the computational experiments as close as possible to a realistic laboratory scenario, while at the same time providing a stringent verification for the modelling assumptions on which the analytical model was built.

While we fix the properties of the upper (+) droplet, we allow for significant variation of the lower drop parameters, with  $V = V_-/V_+$  taking values between 0 and 4, and  $R = R_-/R_+$  having 1 (equally sized droplets) and  $R \rightarrow \infty$  (impact onto a liquid pool) as limiting cases. The latter case requires a dedicated implementation. Referring back to figure 7, symmetry conditions are used on the left-hand side of the domain in order to improve efficiency, while outflow conditions are set on the opposite right-hand side boundary, as well as on the top and bottom boundaries. For the latter of the two, we have carefully examined any potential issues stemming from the fact that for large values of  $R$  the boundary cuts through the drop itself. While locally near the respective boundary the flow is sensitive to the specific choice in condition (stress-free and imposed time- and colour-function dependent vertical velocity have been tested), any details play an inconsequential role at the level of the region of interest in the centre of the domain for the timescales considered here. An extended computational domain with a suitably reduced refinement level may also be used as an alternative solution, maintaining an overall reasonable number of degrees of freedom. The dimensionless size of the finite computational box is set to  $L = 5$  with  $0 \leq x \leq 5$  and  $-2.5 \leq y \leq 2.5$ , which has proven sufficient to track the impact process even beyond early times. Initially we consider the drops to be placed at a small finite distance from one another, such that the centre of



the top drop sits at  $y = 1.025$ , while the lower drop centre is described by  $-R - 0.025V$ , reflecting the variations in both size and velocity. The approach time of the drops is taken to be negative (starting from  $t = -0.025$ ), such that  $t = 0$  coincides to the theoretical time of contact at the  $y = 0$  centreline if there were no deformation of the interfaces. We consider times up to  $t = 0.175$  to cover the early-time evolution appropriate for comparison with analytical results. Detailed flow measurements are taken at every 0.0001 time units for the interfacial shapes, as well as every 0.001 units for all variables of interest (velocities, pressure etc.). This provides a comprehensive dataset spanning 0.2 dimensionless time units, which corresponds to 20  $\mu\text{s}$  in real time. Each direct numerical simulation is run in parallel on 8 CPUs on local high performance computing facilities for approximately 72 hours in wall clock time.

Several steps have been taken to ensure the numerical accuracy of the implementation. Taking advantage of the parallel capabilities of the code through its highly efficient quadtree (or octree in 3D) construction has already been alluded to above. One other key advantage of *Gerris* rests in its ability to represent multi-scale features using versatile adaptive mesh refinement (AMR). As shown in the inset in figure 7, we have taken full advantage of this feature in the region of impingement and liquid jet formation. More generally, the grid resolution varies between levels 9 and 12, with level  $n$  corresponding to  $2^n$  cells per dimension should the grid be uniform. Thus the smallest cell size is  $5/2^{12}$  in our case, which translates to 1.22  $\mu\text{m}$  in dimensional terms. Far away from the impact region this is increased to almost 10  $\mu\text{m}$  in size. A fully uniform grid at the finest resolution would require  $(2^{12})^2 \approx 17 \cdot 10^6$  cells, however with careful refinement imposition we require less than  $5 \cdot 10^5$  cells at any given time in the flow evolution. We prescribe the smallest cell sizes to represent the fluid-fluid interfaces (both liquid-gas and the internal liquid-liquid interface, described in more detail in the following section), and in response to sharp changes in vorticity. Furthermore, we consider a moving rectangular structure which is refined more strongly outside the liquid regions in anticipation of the evolving jet and possible droplet break-off.

In addition to the above, inspired by the careful experimentation of Thoraval (2013) and expanded upon in the associated publications within, we consider a spatial filtering scheme (applied once) to manage the strong contrast in density and viscosity in order to aid convergence of the projection solver, which has also been adapted to include rigorous tolerances at every time step. Finally, to avoid allocating unnecessary resources far away from the impact, jet formation and evolution regions of interest, small droplets and gas bubbles (spanning less than 12 grid cells as  $x < 0.5$  and 32 grid cells as  $x > 0.5$ ) are dynamically removed from the domain by a numerical procedure which effectively replaces the small target fluid region with the surrounding fluid should the imposed criteria be met.

As part of an extensive validation procedure, we have considered several refinement levels in order to verify that the results have converged, with the smallest cell size being varied from level 10 to level 13 for several reference test cases. It was clearly observed that level 10 (yielding cells of size 4.88  $\mu\text{m}$ ) was insufficient for this challenging regime, producing numerical artefacts during the coalescence process and not allowing an appropriate formation of the liquid jet itself. At level 11, the qualitative features were correctly recovered, however quantitatively there were still significant discrepancies when comparing to selected metrics from the analytical model. Moving to level 12 alleviated these issues and good agreement to the predictions has been observed. In order to confirm this, level 13 (corresponding to sub-micron resolution) refinement indicated no further improvement when studying properties of the fully developed jet such as root location, velocities and thickness. We have thus concluded that level 12 suffices for our target

timescales and lengthscales, and the remaining studies in the parameter space have been finalised at the respective resolution level. We emphasise however that the described computational resources are specialised towards resolving the formation and evolution of the liquid jet in view of validating and extending our analytical results. Consequently, more detailed features that have formed the subject of previous investigations such as the structure of the gas entrapment in Thoraval *et al.* (2012) are beyond the reach of the selected numerical configuration and would require additional refinement in the target regions to ensure convergence.

Before proceeding to a systematic study of the splash jet, we note that we have also inspected the early stages of the flow prior to the formation of the jet guided by the recent results of Josserand *et al.* (2016). Whilst the investigation in question is based on axisymmetric calculations (as opposed to two-dimensional here) of impingement onto relatively thin liquid films, several insightful analogies can be constructed by concentrating on the early part of the impact. We find that in our high-speed regime, as suggested by the *jet number* argument of the authors, the jet forms relatively soon after the bubble entrapment takes place. We note that in the centre of the domain near the axis of symmetry we see the formation of a vortex sheet about this bubble (see the inset of figure 7). Perhaps owing to the large velocities considered, we find the structure in question to be very rich (and sensitive to local refinement) close to the centre, however it then becomes smooth roughly half way through to the location of the jet root once the latter appears. By considering the spreading radius as the point of maximal velocity in the flow, we have also verified that the respective instance of jet formation coincides with a significant increase in velocity and that the timescale between when coalescence is first observed and the emergence of the jet is well in line with the prediction of Josserand *et al.* (2016), despite noting again the geometrical discrepancies between the two studies. These conclusions extend from the case of a drop impacting a stationary pool to the symmetric case ( $R = V = 1$ ), as well as the asymmetric cases (e.g.  $R = 2$ ,  $V = 1$ ) we have analysed.

In what follows we elaborate on the comparison between the numerical results obtained with the implementation described above and the analytical findings from the earlier sections of the present work.

## 5. Results and comparisons

In order to conduct a comprehensive comparative study between the asymptotic and the computational results, we focus on the jet root region and along the jet itself. Features related to these structures are extensively characterised in the analytical section of this work. Furthermore, these concentrate some of the most challenging aspects of the physics involved, such as rapid topological changes and large velocities in relatively small areas of the domain. A typical region of interest in the fully developed flow is illustrated in figure 8, where we plot the velocity components and vorticity for the case  $R = 2$  and  $V = 1$ . There are two different sets of curves in each plot: in black, the upper and lower turnover curves defining the liquid-gas interface and in a light grey, a virtual interface between the two liquid drops. The virtual interface is tracked by means of a passive tracer. For this example, the jet curves upwards due to the asymmetry in  $R$ , while the virtual interface allows us to track the contribution of each liquid drop to the jet.

### 5.1. Jet root location

Of primary interest is the correct identification of the jet root location, with the leading-order expressions given in (3.21). To accomplish this, a suitable large subset of the curves

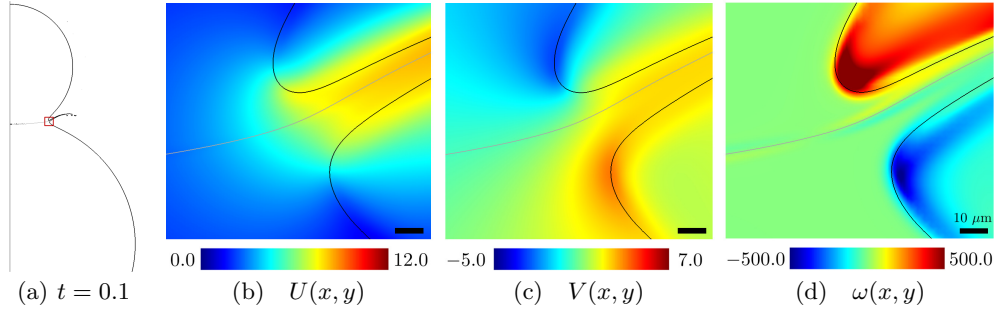


FIGURE 8. Colour online. Horizontal velocity  $U(x, y)$ , vertical velocity  $V(x, y)$  and vorticity  $\omega(x, y)$  inside a selected jet root region for an example solution characterised by  $R = 2$ ,  $V = 1$  at dimensionless time  $t = 0.1$ . a) Liquid-liquid interfaces are shown, while the inset depicts the region of interest illustrated in the figures on the right hand side. Scale bars corresponding to  $10 \mu\text{m}$  are present on the lower right hand corner of each subfigure b)-d).

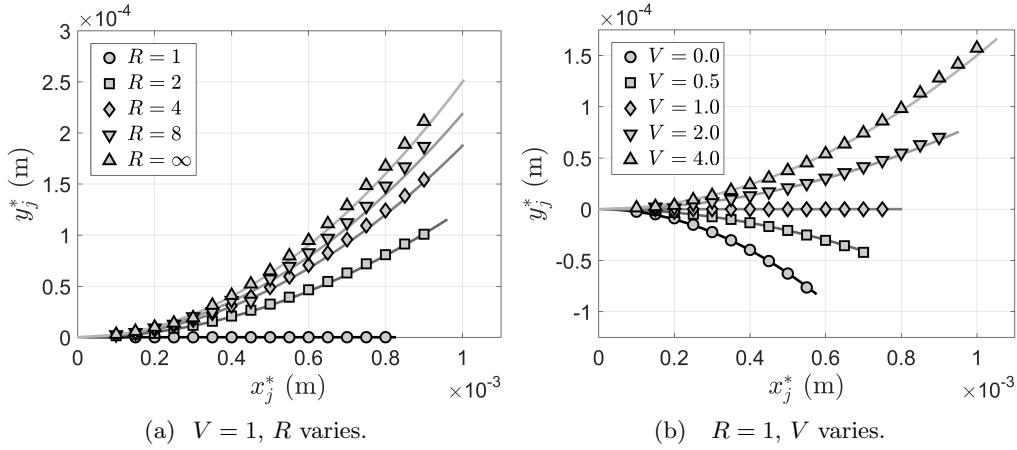


FIGURE 9. Comparison between analytical prediction (3.21) (lines) and numerical results (symbols) for two families of tests: a) Relative impact velocity coincides ( $V = 1$ ), while  $R$  is varied from a case with identical drop size to the limiting case  $R \rightarrow \infty$ , where a drop impacts a liquid pool. b) The relative drop size is set to 1 and the relative impact velocity  $V$  is varied from 0.0 (stationary drop) to 4.0.

around the upper and lower turnover points are selected from the main liquid-gas interface. These are projected and interpolated onto regular grids, as many of the underlying data points are found to be in close proximity to one another due to the very fine grids used. We use a maximum curvature criterion in each local turnover region to then identify the precise location of the turnover points (cf. figure 3). Drawing a line between them, we then consider the intersection of this line with the passive interface as the jet root location to be compared to (3.21). We note that the procedure of identifying the turnover points becomes non-trivial in view of the large parameter space and different aspect ratios and locations of the arising geometrical structures. Consequently, careful post-processing was required to ensure accurate measurements have been considered.

The extracted results (symbols) are plotted alongside the analytically derived jet root location curves in figure 9 for two different families of tests. Note that while the symbols are plotted relatively sparsely, the underlying datasets in each example have 200 points.

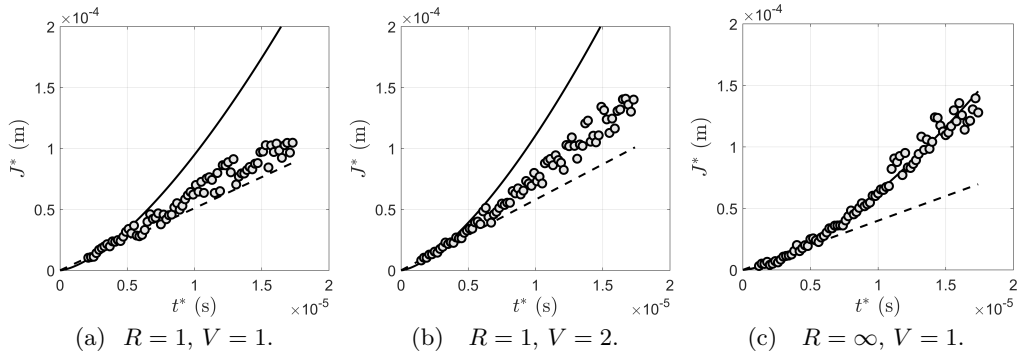


FIGURE 10. Jet root thickness  $J^*$  evolution in time for three different cases in  $R$  and  $V$ . The symbols represent data from direct numerical simulations, while the underlying lines present evolutions proportional to  $(t^*)^a$  that best fit the early stages of the flow. The solid line corresponds to  $a = 3/2$  (the Wagner prediction), while the dashed line indicates linear growth in time as given by  $a = 1$  (the inviscid prediction of Josserand & Zaleski (2003)).

Both sets of coordinates have been re-cast into dimensional variables (hence the (\*) superscripts) to facilitate the comparison. In figure 9a, we keep the impact velocities fixed and equal to one another and vary the radius of the lower drop from a size equal to the upper drop to the limiting case in which the lower liquid region becomes a liquid pool. For  $R = V = 1$ , we find the anticipated horizontal location of the jet root, with the jet root moving away from the lower droplet/pool as  $R$  is increased, as previously observed in figure 5c. In figure 9b, we fix  $R = 1$  and focus on the variation of the impact velocity, with  $0 \leq V \leq 4$ . The data is extracted based on a fixed time window, with the different curve lengths reflecting the jet root coordinate dependence on parameters  $R$  and  $V$ . This is particularly noticeable in figure 9b, in which the presence of  $V$  solely in the numerator of the results summarised in (3.21) translates to an overall movement of the jet root proportional to its value. As alluded to previously in the discussion around figure 5, the non-trivial behaviour of the jet curving either towards or away from the lower drop is recovered depending on the value of  $V$ . Excellent agreement is found across all examined test cases over a generous early time interval spanning the range of validity of the model. In the latter stages, the  $x_j^*$ -coordinate of the jet root location approaches 1 mm in size, which indicates that the jet root location has travelled a distance of almost one full drop radius. At this stage, the leading-order analytical prediction underestimates the numerical results.

## 5.2. Jet root thickness

We move on to investigate the evolution of the dimensional jet thickness,  $J^*$ , in time, where the thickness is measured as the distance between the upper and lower turnover points as seen in figure 3). We recall that, as discussed in §3.3, in Wagner theory the jet thickness must grow like  $t^{*3/2}$ . This is in contrast to growth proportional to  $t^*$  in the inviscid regime suggested by Josserand & Zaleski (2003) for axisymmetric droplet impact onto a thin film. In the same paper, the authors suggest that at early times when  $t \ll t_v = (2R_+/V_+)/\text{Re}$ , viscous effects play the dominant role in the jet thickness, with the appropriate growth rate being proportional to  $t^{*1/2}$ . However, we note that  $t_v \approx 10^{-8}$  s here, so on the timescales we consider in the present paper, we expect the inviscid theory to dominate. In their study of planar droplet impact onto a thin layer, Coppola *et al.*

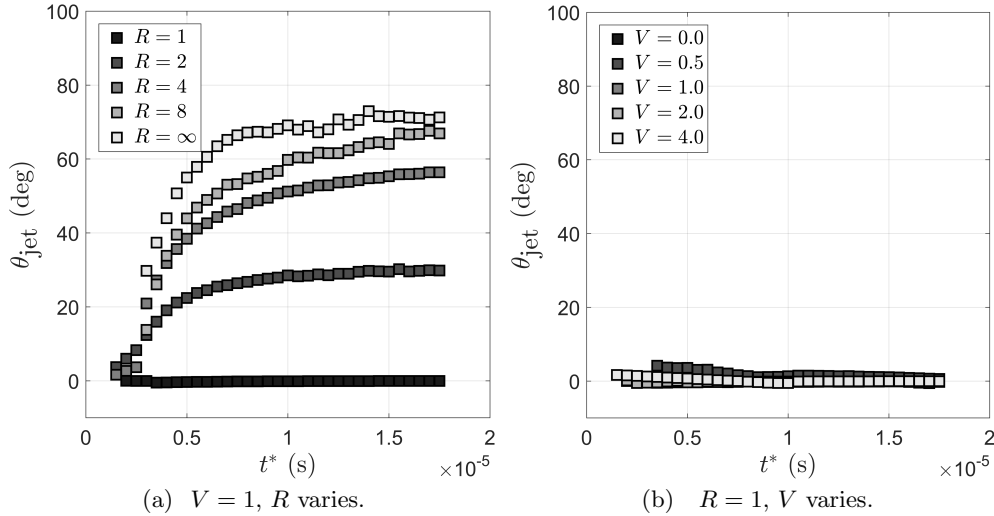


FIGURE 11. Summary of instantaneous jet angle  $\theta_{\text{jet}}$  evolution for two families of tests: a) Relative impact velocity coincides ( $V = 1$ ), while  $R$  is varied from a case with identical drop sizes to the limiting case  $R \rightarrow \infty$ , where a drop impacts a liquid pool. b) The relative drop size is set to 1 and the relative impact velocity  $V$  is varied from 0 (stationary drop) to 4.

(2011) show that the jet thickness is approximately linear at later times, although they also show that the horizontal projection of the jet thickness grows like  $t^{*3/2}$ .

We wish to investigate this in more detail for various values of  $V$ ,  $R$  and we plot the results in figure 10. In the first plot, we consider the symmetric case  $R = V = 1$ , where we see  $J^*$  exhibiting faster than linear growth, albeit significantly undershooting growth proportional to the prediction of leading-order Wagner theory. If the velocity ratio is increased, the thickness growth is now clearly faster than linear, although again there appears to be a deviation away from  $t^{*3/2}$  for larger times. In the final example, for droplet impact onto a liquid pool (with  $R = \infty$  and  $V = 1$  in subfigure 10(c)), the jet thickness clearly follows the Wagner prediction over several decades.

Overall, there is strong evidence that the jet thickness grows more rapidly than the linear prediction of Josserand & Zaleski (2003), but in some cases more slowly than the predictions of Wagner theory. It may be that other physical effects play a role in thinning the jet: the highly-curved free surfaces cause a build up of vorticity in the jet root (see figure 8(d), so that viscous and capillary effects may play a role that cannot be picked up by the inviscid theory. However, the clear evidence in the third example of figure 10 that the jet thickness grows like  $t^{*3/2}$  suggests that there are regimes in which the Wagner prediction is valid.

### 5.3. Jet angle

The jet angle,  $\theta_{\text{jet}}$ , was introduced in figure 3 as the instantaneous angle between the tangent to the interface between the two droplets and the horizontal at the point at which the line joining the upper and lower turnover points intersects the interface. In §3.3, we discussed the difficulties in predicting this angle using Wagner theory, with the only sensible prediction of the jet angle being given by  $\alpha$  in (3.24), which is the slope of the vortex sheet in the outer region as it approaches the turnover point. In this section, we shall investigate the evolution of  $\theta_{\text{jet}}$  for several different impact scenarios and we shall consider whether  $\alpha$  is a reasonable estimation of the jet angle.

To extract  $\theta_{\text{jet}}$  numerically, at each instance in time we consider the point defining the root of the jet on the virtual interface between the two fluids. We then move ahead in a discrete sense, selecting another point further ahead along the jet and thus enabling us to define an angle with the horizontal axis. We have experimented with the choice in this reference point in order to study how the degree of locality affects the jet angle. In particular, we have varied our spatial window from one point ahead to 16 virtual points ahead, which for our resolution gives us a distance between  $0.25 \mu\text{m}$  to approximately  $4 \mu\text{m}$ . Fig. 8b-d provides an indication of the bending of this jet and hints at the variability of the angle depending on the choice of reference points. To illustrate this aspect, we will refer to specific cases in more detail, however in terms of summarising the datasets we have selected the 16 point heuristic as being sufficiently robust, with the outcomes presented in figures 11–13.

In figure 11, we plot the evolution of  $\theta_{\text{jet}}$  as a function of the dimensional time for the first 17.5 microseconds of the impact. When we fix the ratio of the impact velocities at  $V = 1$  and vary  $R$  in figure 11a, we see a strong variation from the horizontal jet predicted when the impact is completely symmetric with  $R = 1$  (a prediction that is consistent with (3.24)). For  $R > 1$ , we see  $\theta_{\text{jet}} \sim \sqrt{V_+ t^*/R_+}$ , a growth-rate predicted by Thoroddsen *et al.* (2011) — and indeed by (3.24) — using a simple geometric model. It is worth reiterating that the exact definition of the jet angle is important. Thoraval *et al.* (2012) take the angle to be that between the normal to the line between the turnover points and the horizontal in their study of droplet impact onto a deep pool. Over timescales similar to those we study here that angle grows linearly in time.

In contrast, in figure 11b, we fix the ratio of the radii of curvature at  $R = 1$  and vary the impact speed ratio,  $V$ . Perhaps surprisingly, we see that, even for starkly different impact speeds, when  $R = 1$ , the jet is essentially emitted horizontally, which is consistent with the Wagner prediction, (3.24). Therefore, even though vorticity will undoubtedly build up on the jet root free surfaces, see for example figure 8d, and will play a role in the jet angle evolution when  $R \neq 1$  (as we discuss shortly), perhaps the largest contributing factor to the angle at which the jet is emitted is the ratio of the droplet radii of curvature.

We now move on to compare  $\theta_{\text{jet}}$  with  $\alpha$  by carefully examining two particular cases in more detail, with the results displayed in figures 12–13. In these figures, we provide a comparison between the Wagner prediction for the leading-order jet angle as given by (3.24) and the numerically measured angle,  $\theta_{\text{jet}}$ . At the same time, we also describe the methodology behind the results analysis in §5.1 in more depth.

Firstly, guided by relation (3.24) and figure 11, we investigate a case which is predicted to have a horizontally evolving jet despite an asymmetric  $R/V$  configuration, with  $R = 1$  and  $V = 2$ . In figure 12a, we not only show the jet root coordinate evolution alongside the analytical prediction as before, but also present the identified turnover points its detection is based on. In figure 12b, we plot the analytic prediction of the jet angle as given by  $\alpha$  in (3.24), while in figure 12c, we display the numerically measured angle  $\theta_{\text{jet}}$  for each of the 1-, 4- and 16-point reference choices. For this case, where the jet is essentially emitted horizontally, there is very little difference between these choices, and it is clear that both the analytic and numerical jet angles agree.

In figure 13, however, we see somewhat different results. In this example, we have chosen  $R = 3$ ,  $V = 0$  — note that this leads to a horizontal jet root coordinate of  $y_j = 0$  (cf. (3.22)). Firstly, we note that, despite the apparent noise in the data in figure 13a, the jet root coordinate varies within roughly  $1\text{--}2 \mu\text{m}$  throughout its evolution, which is at the level of the grid cells used in the direct numerical simulations. Thus, given the sensitivity of this particular case in light of the fine balance between the impinging drop sizes and velocities, the result is actually very accurate. However, when comparing the vortex sheet

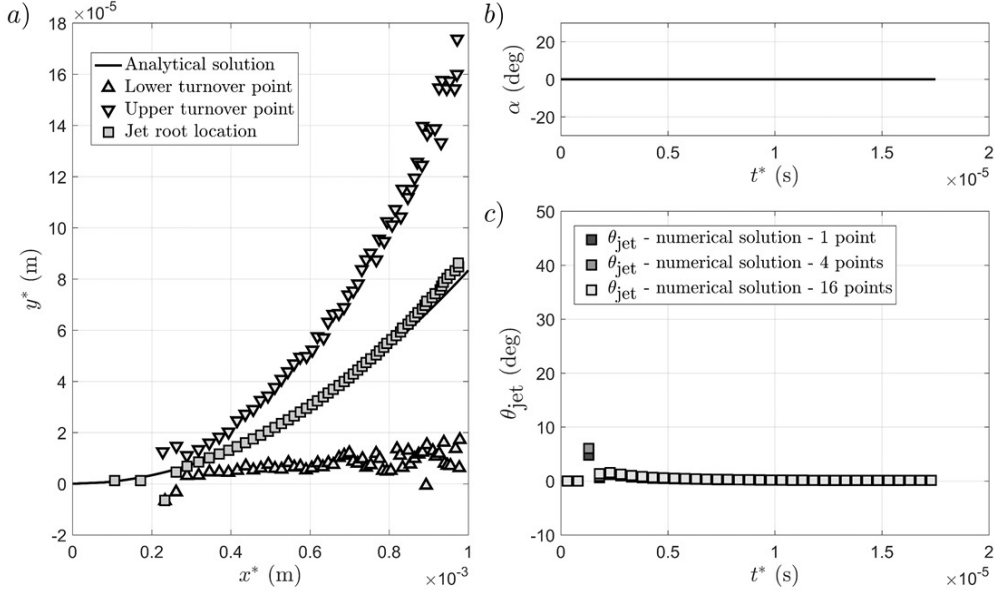


FIGURE 12. Summary of the jet root evolution for the case described by  $R = 1$  and  $V = 2$ . a) The identified lower and upper turnover points along with the associated jet root coordinates, with the symbols denoting the numerically obtained results and the continuous line illustrating the analytical prediction as given by 3.21. b) the inviscid estimate of the jet angle,  $\alpha$  previously derived as expression (3.24). c) instantaneous jet angle  $\theta_{\text{jet}}$  obtained numerically using distance criteria based on including either 1, 4 or 16 virtual interface points ahead of the jet root in order to calculate the angle the jet makes with the horizontal axis.

angle  $\alpha$  (depicted in figure 13b) and the measured instantaneous jet angle  $\theta_{\text{jet}}$  seen in figure 13c, we see that the Wagner prediction significantly underestimates the jet angle — by about a factor of two — although both figures capture the square-root growth of the angle in time. We postulate that this discrepancy is due to the role of vorticity (and, to a lesser extent, surface tension) in the inner region. Moore *et al.* (2014) discuss the boundary layers induced by the highly-curved free surface in the Wagner inner region, and it is well-known from previous works in the area, for example Thoraval *et al.* (2012), Thoraval *et al.* (2013), that vorticity build up on the free surface can even lead to vortex shedding and the formation vortex streets. Moreover, the vorticity build-up can readily be seen in figure 8c, with the dimensionless vorticity  $\omega$  varying from approximately  $-500$  at the lower jet root to  $500$  at the upper jet root at  $t = 0.1$ . We believe that the angle of the jet is strongly influenced by this significant vorticity, with the jet angle increasing with time (so that the jet is emitted closer to the upper drop in this example) due to an imbalance in the magnitude of the vorticity at each jet root. This is also reported by Thoraval *et al.* (2012) who find the instantaneous maximum positive and negative vorticities in the impact of a droplet onto a deep pool. They find these extremal values occur near the upper and lower turnover points respectively, with a marked difference in the numerical values. In that example the jet angle increases sufficiently rapidly so as to impact on the side of the droplet (“bumping”), causing bubble entrapment.

Nevertheless, when considering the examples in which  $R = 1$ , it appears that the ratio of the droplet radii of curvature also plays an important role the increase in  $\theta_{\text{jet}}$  with time: when  $R = 1$  there are still large vorticities associated with the highly-curved free surface local to the jet root, but the jet remains approximately horizontal for the duration

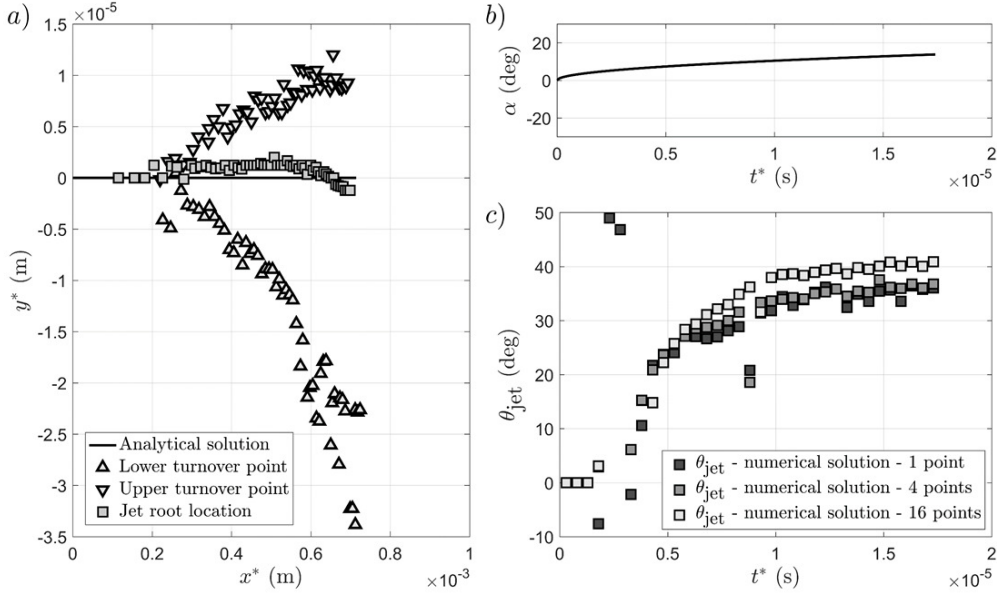


FIGURE 13. Summary of the jet root evolution for the case described by  $R = 3$  and  $V = 0$ . a) The identified lower and upper turnover points along with the associated jet root coordinates, with the symbols denoting the numerically obtained results and the continuous line illustrating the analytical prediction as given by 3.21. b) Jet-root region angle  $\theta_j$ , with the analytical result previously derived as expression (3.24). c) instantaneous jet angle  $\theta_{\text{jet}}$  obtained numerically using distance criteria based on including either 1, 4 or 16 virtual interface points ahead of the jet root in order to calculate the angle the jet makes with the horizontal axis.

of our simulations. Both of these assertions warrant further investigation, although we do not aim to pursue such an analysis here. What is clear however, is that Wagner theory cannot accurately predict the angle at which the jet is emitted, aside for cases in which the droplets have comparable radii of curvature.

We note that figure 13c also indicates how sensitive the measurement of  $\theta_{\text{jet}}$  is to the choice of reference points: the 1- and 4-point based datasets resulting in lower angle values. Finally, in all cases the nature of the instantaneous jet angle calculation method results in strong variability in the early stages of jet formation, should the jet be so small that the necessary number of points is not available and hence the reference point is selected further along the interface and into the main body of the drop.

#### 5.4. Jet velocity and thickness

We now move on to consider the jet itself, in particular concentrating on the jet shape and velocity at various stages of the impact. We present our findings in figure 14 for the  $R = 2$  and  $V = 1$  case. In figure 14a we employ a different visualisation technique to overlay not only the leading-order jet root locations, but also the full numerically-obtained jet shapes up to when the liquid begins to thicken and form the tip. The more pronounced bend in the jet becomes visible as we advance towards this region, especially in the latter stages. The respective curves are constructed from the virtual interface given when considering the passive tracers in the flow. These have previously been shown as part of figure 8 (in light grey) and they may be used as an indication of the top and bottom liquid contributions into the jet. We note that in most asymmetric cases (in either  $R$  or  $V$ , or both) we anticipate this virtual interface not to be aligned with what can be defined as a geometrically central curve along the jet, an aspect which is not accounted



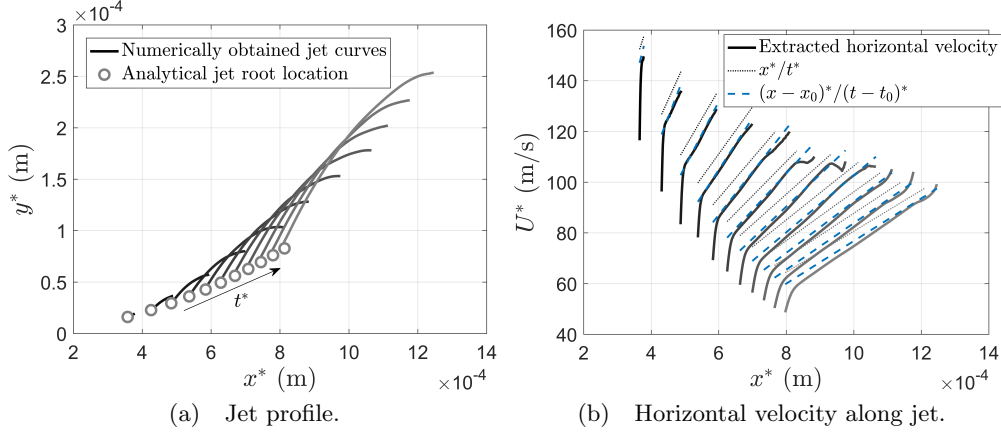


FIGURE 14. a) Evolution of the jet for  $R = 2$  and  $V = 1$  from the time of its creation at  $t^* = 2.4 \times 10^{-6}$  s to  $t^* = 1.24 \times 10^{-5}$  s in increments of  $1.0 \times 10^{-6}$  s. The full shape up to the jet tip is extracted from the direct numerical simulations, while the coordinates of the jet root as obtained analytically are also presented. b) Dimensional horizontal velocity  $U^*(x^*, t^*)$  for each time step and comparison to the leading-order Wagner solution (3.34). Both a direct comparison (dotted line) and a simple correction to account for the presence of the entrapped gas bubble (dashed line) are illustrated.

for in the analytical model, which cannot predict non-symmetric contributions from the two droplets to the fluid in the jet at leading order.

Typical jet velocity profiles extracted at the coordinates given by such curves are shown in figure 14b. Close to the jet root, there is a large initial increase in the velocity consistent with the large velocity scales in §3.3. The velocity subsequently falls into a regime of linear growth, which compares favourably to the predicted leading-order tangential jet velocity profile given by (3.34), particularly for earlier times. With the reference impact velocity at 10 m/s, we find velocities along the jet are larger by an order of magnitude in the tested conditions, with a steady overall decrease as time advances. We note that this type of linear dependence is also discernible in the potential flow calculations of Riboux & Gordillo (2017), although in that paper, the authors have concentrated their attention on the characterisation of the boundary layer properties preceding the location of the jet root.

It should be noted that initially the results have not been modified or adjusted at the root of the jet to aid the comparison (represented through the dotted lines). The small gap between the curves for smaller times is believed to be associated with the existence of the trapped gas bubble, which is present in the full numerical setup, but ignored in the analysis. We opted to illustrate the unaltered results to enable a clean contrast between the analytical predictions and the direct numerical simulation. Especially for the first few sets of curves, the slopes compare favourably. This is to be expected, as we are well within the regimes in which the asymptotic solution is valid. At later stages and sufficiently far into the jet, the agreement begins to deteriorate as the numerically obtained velocity starts to deflect away from the linear behaviour. This is an indication of further physical effects coming into play, for example the interaction of the jet with the surrounding gas. Having established the above, a corrective step similar to that undertaken by Philippi *et al.* (2016) consisting in a temporal and spatial adjustment accounting for the slight delay and shift in location of the coalescence is then conducted, using  $t_0$  and  $x_0$  to denote these offsets in figure 14b. This results in significant improvement of the overall

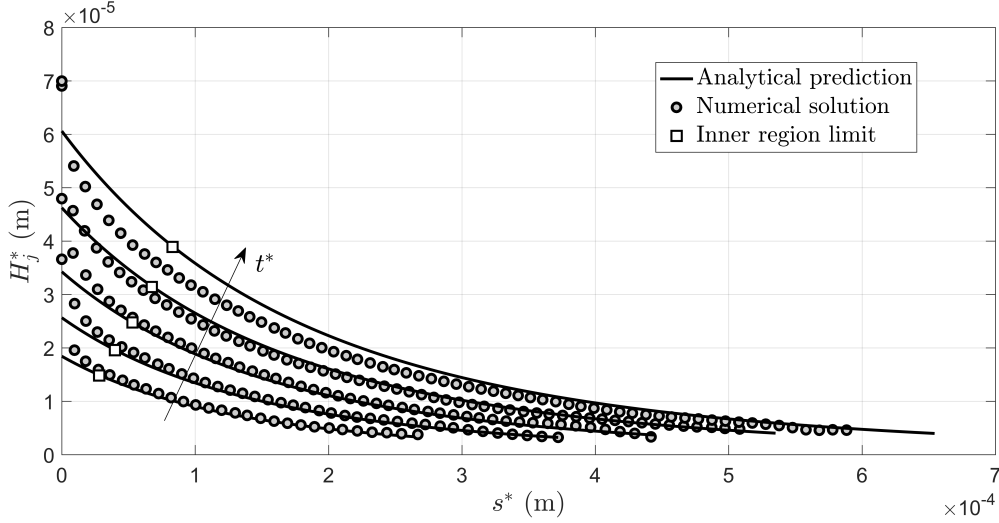


FIGURE 15. Evolution of the jet thickness for the case described by  $R = 2$  and  $V = 1$  illustrated at five instances in time, from  $t^* = 6.7 \times 10^{-6}$  s to  $t^* = 1.47 \times 10^{-5}$  s in increments of  $2.0 \times 10^{-6}$  s. The grey symbols indicate results extracted from direct numerical simulations, while the solid lines represent the associated analytical predictions as given by expression 3.34. The leading-order jet thickness as given by analysing the inner region, previously derived as equation (3.29), is also presented in each case using white squares.

agreement and in particular for the early stages of the jet evolution, where any differences are essentially indistinguishable.

We found it significant that in this regime one of the classical definitions of the spreading radius as the point of maximal velocity in the flow becomes somewhat ambiguous. The increasing velocity inside the jet and the details around the tip of this structure dictate the outcome under this metric. This does not appear to be the case in lower speed impact scenarios, which select a point near the jet root as having this property, see for example Thoraval *et al.* (2012) and Josserand *et al.* (2016).

Finally we explore the thickness of the jet in detail and concentrate on the  $R = 2$ ,  $V = 1$  case in figure 15. In section 3.4 we derived an analytical result based on Wagner theory for the leading-order jet thickness  $\bar{\chi}_0$ , (3.34), predicting a variation of  $\bar{s}^{-5}$  along the jet where  $\bar{s}$  is the arc length coordinate along the jet. The figure illustrates several such curves considered equidistantly in time, alongside the points delimiting the inner region from the jet region (in white squares). Alongside these we present the corresponding numerical results, which are calculated as follows. We start from the jet root coordinate and the identified lower/upper turnover points used to calculate it. The distance between them forms the first natural thickness measurement. For the next thickness result along the jet, we move along the virtual interface by one discrete point and provide a subset of data points immediately ahead of the turnover regions from which we select the nearest distance candidates to the virtual interface point, both above and below. We then iterate on this procedure, marching forward along the jet whilst also sliding the candidate points above and below. The data extraction is halted once a significant jet thickening is observed, indicative of the presence of the tip. As may be anticipated, the specific parameter choices such as the size of the candidate points intervals does indeed affect the first few thickness measurements, however we found that beyond these first points along the jet, the algorithm becomes robust in the sense of the estimated thickness being

insensitive to parametric changes. Consistently, the threshold point roughly corresponds to the identified limit of the inner region and start of the jet region.

As is clear from figure 15, the agreement between Wagner theory and the numerical simulations is excellent, which is perhaps surprising as the Wagner jet does not take any effects of the tip into account. Among others, Thoroddsen (2002), Josserand & Zaleski (2003), Riboux & Gordillo (2015) and Josserand *et al.* (2016) discuss the motion of the jet tip, with strong indication that its motion is governed by not only the liquid viscosity and surface tension but also the action of the surrounding gas. Despite the present study considering flow regimes towards the inviscid limit of the parameter spaces in the respective investigations (either through the selection of water as opposed to high viscosity water-glycerine mixtures or through the consideration of comparatively larger impact velocities), it is likely that the decrease in accuracy of the inviscid jet model as time increases is a result of these effects on the jet tip, or indeed along the whole jet, as considered by Moore & Oliver (2018).

### 5.5. Summary

In summary, the comparisons between the full numerical simulations and the leading-order analytical predictions are extremely encouraging. As discussed in Riboux & Gordillo (2014), Riboux & Gordillo (2015) and Philippi *et al.* (2016), it is well-known that Wagner theory provides a good estimation of the size of the effective contact set in droplet impact onto a solid substrate. Here, we have shown that this is also true for the liquid-liquid regime for a range of droplet diameters and impact speeds, as evidenced in figure 9. Moreover, we have shown that Wagner theory also gives a reliable estimate of the elevation of the jet root and the shape of the curve mapped out by the jet root, as shown in figure 14a. There is also good (subject to a consideration of the role of the entrapped central gas bubble present in the full model) agreement between the predicted leading-order jet velocity and the full numerical simulations in figure 14b. Furthermore, there is also excellent agreement between the predicted leading-order jet thickness and the numerical solution, as seen in figure 15.

All of these comparisons indicate that in any investigation of the behaviour of the ejecta in droplet impacts, we can reliably use Wagner theory as a basis for prescribing initial conditions for the jet root location and fluid velocity. This has the potential to make analysis of jet evolution much simpler, as we can neglect the flow in the bulk of the droplet and investigate interactions between the fast-moving jet and the surrounding gas in greater detail.

We do, however, need to be slightly more cautious when considering the jet thickness and angle. In terms of the jet thickness, we saw in figure 10 that although there was strong evidence of the jet thickness growing more rapidly than linearly with time, it was only for large values of  $R$  (i.e. as we approach impact onto a deep pool) that the characteristic Wagner  $t^{3/2}$ -growth was seen over a long range of times. It is possible that for smaller values of  $R$ , other physical factors such as the role of viscosity or surface tension on the highly-curved jet surfaces cause deviations from the inviscid prediction of the jet thickness.

We encounter similar problems when considering the jet angle. In cases where the ratio of the droplet radii of curvature is close to unity, both the theory and the numerical simulations predict that the jet is approximately horizontal, see figure 11 and figure 12b-c. However, as the ratio increases, the difference in the vorticity building up on the highly-curved jet root free surfaces appears to lead the jet angle to increase much more quickly than Wagner theory predicts, as displayed in figure 13b-c. Naturally this phenomenon cannot be captured by the purely inviscid theory and it appears a more careful analysis

of the full Navier-Stokes equations is required to capture this behaviour, in a similar manner to Moore *et al.* (2014), who consider the capillary and viscous boundary layers in the jet root region in liquid-solid impact. We do note, however, that although there is a noticeable influence of the vorticity build-up on the jet angle, there is at this stage no evidence of the vortex streets seen in similar computations, see for example Thoraval *et al.* (2012) (with the usual caveat that we are considering a two-dimensional problem here, rather than axisymmetric). Despite this, as we observe in figure 14a, the jet is already curving downstream of the jet root, indicating that this deflection is likely not a product of vorticity shedding. It is an open question as to what causes jet bending, but it is probable that the surrounding gas plays a critical role, as described through a simple kinematic model and via comparison with low pressure experiments by Thoroddsen *et al.* (2011), as well as recently discussed in Moore & Oliver (2018).

From a more general viewpoint, the validation has proven robust across a wide range of parameters and in various flow regions. Despite the differences in the two setups (presence of a trapped gas bubble, presence of surrounding gas, surface tension, gravity), the qualitative and, more importantly, quantitative validation of the asymptotically predicted structures has been successfully addressed. Furthermore, features beyond the analytically tractable arguments have been discussed through the use of full numerical results.

## 6. Conclusion

In this paper we have performed an in-depth analytical and numerical investigation into the vertical impact of two-dimensional liquid droplets of the same fluid. We employed full numerical simulations of the two-fluid Navier-Stokes equations to assess the veracity of the classical Wagner solution at early stages of the impact. Our particular concern has been with the location of the root of the jet of fast-moving fluid that is emitted after impact and we have shown that there is excellent agreement between the predictions of the Wagner model and the numerical solution. In addition, we obtained good agreement for the speed of the fluid in the jet and the jet thickness between the model and the simulations for a wide range of droplet radii and velocities.

While not expanded upon in the previous section, we have also experimented with higher viscosity liquids in order to attempt to clarify the large Reynolds number restriction and investigate the influence of this parameter on the properties of the development of the flow. At an order of magnitude below the main set of results presented here (with  $Re \approx 10^3$  rather than  $10^4$ ), we have observed minimal differences in the jet root locations, while, arguably intuitively, a slight slowing down of the timescale of the jet angle evolution to the same final values and a thickening of the jet have also been observed. Despite having pushed towards a region of the parameter space which lies at the edge of the validity of the analytical model, it still showed remarkable robustness.

The implications of this successful qualitative and quantitative validation of the Wagner model is twofold. Firstly it gives us further confidence in the accuracy of the numerical simulations shortly after impact, where there are rapid topological changes as the ejecta forms, which follows on from the existing works in the field, for example Coppola *et al.* (2011), Thoraval *et al.* (2012), Riboux & Gordillo (2014), Riboux & Gordillo (2015) and Philippi *et al.* (2016). Secondly, it also indicates that validity of using the predictions of the Wagner model in local analyses of the jet root. For some time, an open question in the literature has been the influence of vorticity shedding on both the accuracy of the Wagner model and the behaviour of splash jets in liquid-liquid impacts. In this paper we show that, certainly for problems where the non-dimensional numbers are of the same order of magnitude as (4.1), the Wagner model still gives an excellent approximation of the

jet root location and speed over timescales in which the jet is first seen to bend, although Wagner theory is less reliable in terms of the jet angle. Nevertheless, the very good agreement between the theory and the simulations for the jet root location and speed, and the jet velocity and thickness is extremely encouraging, and likely to be of benefit in future studies of the behaviour of the jet and its interaction with the surrounding environment.

We have only considered a certain class of problems in this paper and there is much scope for future work. Of particular interest are extensions to axisymmetric and three-dimensional impacts – although Wagner theory is certainly more challenging in the latter, see for example Scolan & Korobkin (2001); Korobkin & Scolan (2006) – as well as incorporating an oblique impact velocity, which may be of relevance in aerodynamic applications, see Cimpeanu & Papageorgiou (2018).

### Acknowledgements

The authors would like to thank Prof. J. M. Oliver for discussions related to the inner region in §3.3. R.C. was partly supported by EPSRC grants EP/K041134/1 and the Mathematical Institute at the University of Oxford. R.C. also acknowledges the infrastructure support and resources provided by the Imperial College London High Performance Computing Service (doi: 10.14469/hpc/2232). The authors would like to thank the anonymous referees whose comments helped improve upon a previous version of this manuscript.

### Appendix A. Outer-outer region

When  $x, y = O(1)$ , the droplets retain their circular shape to leading order and move according to their initial conditions, so that if  $f_{\pm}(x, y, t)$  represents shape of the upper and lower droplets and we expand

$$\phi_{\pm} = \phi_{\pm 0} + \delta\phi_1 + o(\delta), f_{\pm} = f_{\pm 0} + \delta f_{\pm 1} + o(\delta) \quad (\text{A } 1)$$

as  $\delta \rightarrow 0$ , the leading-order solution is simply

$$\phi_{+0} = -y, \quad \phi_{-0} = Vy, \quad f_{+0} = x^2 + (y - 1)^2 - 1, \quad f_{-0} = x^2 + (y + R)^2 - R^2. \quad (\text{A } 2)$$

The  $O(\delta)$ -perturbation to this is driven by the far-field dipoles from the leading-order complex potential (3.13) in the outer region as discussed in §3.2. The appropriate solution is given by

$$\phi_{+1} = \frac{(1 + V)d_0^2}{8} - \left(\frac{1 + V}{4}\right) \frac{d_0^2 y}{x^2 + y^2}, \quad (\text{A } 3)$$

$$\phi_{-1} = \frac{(1 - V^2)t}{2} + \frac{(1 + V)d_0^2}{8R} - \left(\frac{1 + V}{4}\right) \frac{d_0^2 y}{x^2 + y^2}, \quad (\text{A } 4)$$

which gives the following expressions for  $F(t)$  and  $G(t)$ :

$$F(t) = \frac{(1 + V)d_0^2}{8}, \quad G(t) = \frac{(1 - V^2)t}{2} + \frac{(1 + V)d_0^2}{8R}, \quad (\text{A } 5)$$

so that it is clear that  $F, G = O(\delta)$ , as stated in §3.2.

### REFERENCES

- AGBAGLAH, G., THORAVAL, M.-J., THORODDSEN, S. T., ZHANG, L. V., FEZZAA, K. & DEEGAN, R. D. 2015 Drop impact into a deep pool: vortex shedding and jet formation. *J. Fluid Mech.* **764**.
- ARMAND, J.-L. & COINTE, R. 1987 Hydrodynamic impact analysis of a cylinder. *ASME J. Offshore Mech. Arc. Eng.* **111**, 109–114.
- CASTREJÓN-PITA, A. A., CASTREJÓN-PITA, J. R. & HUTCHINGS, I. M. 2012 Experimental observation of von kármán vortices during drop impact. *Phys. Rev. E* **86** (4), 045301.
- CIMPEANU, R. & PAPAGEORGIOU, D. T. 2018 Three-dimensional high speed drop impact onto solid surfaces at arbitrary angles. *Int. J. Multiphase Flow*, accepted, article in press .
- COPPOLA, G., ROCCO, G. & DE LUCA, L. 2011 Insights on the impact of a plane drop on a thin liquid film. *Phys. Fluids* **23** (2), 022105.
- HICKS, P. D. & PURVIS, R. 2010 Air cushioning and bubble entrapment in three-dimensional droplet impacts. *J. Fluid Mech.* **649** (1), 135–163.
- HICKS, P. D. & PURVIS, R. 2013 Liquid–solid impacts with compressible gas cushioning. *J. Fluid Mech.* **735**, 120–149.
- HOWISON, S. D., OCKENDON, J. R., OLIVER, J. M., PURVIS, R. & SMITH, F. T. 2005 Droplet impact on a thin fluid layer. *J. Fluid Mech.* **542**, 1–23.
- HOWISON, S. D., OCKENDON, J. R. & WILSON, S. K. 1991 Incompressible water-entry problems at small deadrise angles. *J. Fluid Mech.* **222**, 215–230.
- JIAN, Z., JOSSERAND, C., POPINET, S., RAY, P. & ZALESKI, S. 2018 Two mechanisms of droplet splashing on a solid substrate. *J. Fluid Mech.* **835**, 1065–1086.
- JOSSERAND, C., RAY, P. & ZALESKI, S. 2016 Droplet impact on a thin liquid film: anatomy of the splash. *J. Fluid Mech.* **802**, 775–805.
- JOSSERAND, C. & THORODDSEN, S. T. 2016 Drop impact on a solid surface. *Ann. Rev. Fluid Mech.* **48**, 365–391.
- JOSSERAND, C. & ZALESKI, S. 2003 Droplet splashing on a thin liquid film. *Phys. Fluids* **15** (6), 1650–1657.
- KOLINSKI, J. M., MAHADEVAN, L. & RUBINSTEIN, S. M. 2014 Lift-off instability during the impact of a drop on a solid surface. *Phys. Rev. Lett.* **112**, 134501.
- KOLINSKI, J. M., RUBINSTEIN, S. M., MANDRE, S., BRENNER, M. P., WEITZ, D. A. & MAHADEVAN, L. 2012 Skating on a film of air: Drops impacting on a surface. *Phys. Rev. Lett.* **108**, 074503.
- KOROBKIN, A. A. 1985 Initial asymptotic behavior of a solution to the three-dimensional problem concerning the entry of a blunt body into an ideal fluid. *Doklady Akademii Nauk SSSR* **283**, 838–842.
- KOROBKIN, A. A. 2007 Second-order wagner theory of wave impact. *J. Eng. Math.* **58** (1), 121–139.
- KOROBKIN, A. A. & SCOLAN, Y.-M. 2006 Three-dimensional theory of water impact. Part 2. Linearized Wagner problem. *J. Fluid Mech.* **549**, 343–374.
- LANGLEY, K. R., LI, E. Q. & THORODDSEN, S. T. 2017 Impact of ultra-viscous drops: air-film gliding and extreme wetting. *J. Fluid Mech.* **813**, 647–666.
- LI, E. Q., LANGLEY, K. R., TIAN, Y. S., HICKS, P. D. & THORODDSEN, S. T. 2017 Double contact during drop impact on a solid under reduced air pressure. *Phys. Rev. Lett.* **119** (21), 214502.
- LI, E. Q. & THORODDSEN, S. T. 2015 Time-resolved imaging of a compressible air disc under a drop impacting on a solid surface. *J. Fluid Mech.* **780**, 636–648.
- LI, E. Q., VAKARELSKI, I. U. & THORODDSEN, S. T. 2015 Probing the nanoscale: the first contact of an impacting drop. *J. Fluid Mech.* **785**.
- LIU, T., TAN, P. & XU, L. 2015 Kelvin-Helmholtz instability in an ultrathin air film causes drop splashing on smooth surfaces. *Proc. Nat. Acad. Sci.* **112** (11), 3280–3284.
- MANDRE, S. & BRENNER, M. P. 2012 The mechanism of a splash on a dry solid surface. *J. Fluid Mech.* **690**, 148–172.
- MANDRE, S., MANI, M. & BRENNER, M. P. 2009 Precursors to splashing of liquid droplets on a solid surface. *Phys. Rev. Lett.* **102**, 134502.
- MANI, M., MANDRE, S. & BRENNER, M. P. 2010 Events before droplet splashing on a solid surface. *J. Fluid Mech.* **647**, 163–185.

- MARTIN, G. D., HOATH, S. D. & HUTCHINGS, I. M. 2008 Inkjet printing - the physics of manipulating liquid jets and drops. *J. Phys. Conf. Series* **105** (1), 012001.
- MOORE, M. R., HOWISON, S. D., OCKENDON, J. R. & OLIVER, J. M. 2012 Three-dimensional oblique water-entry problems at small deadrise angles. *J. Fluid Mech.* **711**, 259–280.
- MOORE, M. R., OCKENDON, H., OCKENDON, J. R. & OLIVER, J. M. 2014 Capillary and viscous perturbations to helmholtz flows. *J. Fluid Mech.* **742**, R1.
- MOORE, M. R., WHITELEY, J. P. & OLIVER, J. M. 2018 On the deflection of a liquid jet by an air-cushioning layer. *J. Fluid Mech.* **846**, 711–751.
- MURPHY, D. W., LI, C., D’ALBIGNAC, V., MORRA, D. & KATZ, J. 2015 Splash behaviour and oily marine aerosol production by raindrops impacting oil slicks. *J. Fluid Mech.* **780**, 536–577.
- OLIVER, J. M. 2002 Water entry and related problems. *DPhil Thesis, University of Oxford*.
- OLIVER, J. M. 2007 Second-order wagner theory for two-dimensional water-entry problems at small deadrise angles. *J. Fluid Mech.* **572**, 59–85.
- PHILIPPI, J., LAGRÉE, P.-Y. & ANTKOWIAK, A. 2016 Drop impact on a solid surface: short-time self-similarity. *J. Fluid Mech.* **795**, 96–135.
- POPINET, S. 2003 Gerris: A tree-based adaptive solver for the incompressible Euler equations in complex geometries. *J. Comput. Phys.* **190**, 572.
- POPINET, S. 2009 An accurate adaptive solver for surface-tension-driven interfacial flows. *J. Comput. Phys.* **228**, 5838.
- PURVIS, R. & SMITH, F. T. 2005 Droplet impact on water layers: post-impact analysis and computations. *Phil. Trans. Roy. Soc. A* **363**, 1209–1221.
- RIBOUX, G. & GORDILLO, J. M. 2014 Experiments of drops impacting a smooth solid surface: A model of the critical impact speed for drop splashing. *Physical Rev. Lett.* **113** (2), 024507.
- RIBOUX, G. & GORDILLO, J. M. 2015 The diameters and velocities of the droplets ejected after splashing. *J. Fluid Mech.* **772**, 630–648.
- RIBOUX, G. & GORDILLO, J. M. 2017 Boundary-layer effects in droplet splashing. *Phys. Rev. E* **96** (1), 013105.
- DE RUITER, J., VAN DEN ENDE, D. & MUGELE, F. 2015 Air cushioning in droplet impact. II. Experimental characterization of the air film evolution. *Phys. Fluids* **27**, 012105.
- SAFFMAN, P. G. 1992 *Vortex dynamics*. CUP.
- SCOLAN, Y.-M. & KOROBKIN, A. A. 2001 Three-dimensional theory of water impact. Part 1. Inverse Wagner problem. *J. Fluid Mech.* **440**, 293–326.
- SEMENOV, Y. A., WU, G. X. & KOROBKIN, A. A. 2015 Impact of liquids with different densities. *J. Fluid Mech.* **766**, 5–27.
- SEMENOV, Y. A., WU, G. X. & OLIVER, J. M. 2013 Splash jet generated by collision of two liquid wedges. *J. Fluid Mech.* **737**, 132–145.
- SMITH, F. T., LI, L. & WU, G. X. 2003 Air cushioning with a lubrication/inviscid balance. *J. Fluid Mech.* **482**, 291–318.
- THORAVAL, M.-J. 2013 Drop impact splashing and air entrapment. PhD thesis, KAUST.
- THORAVAL, M.-J., TAKEHARA, K., ETOH, T. G., POPINET, S., RAY, P., JOSSERAND, C., ZALESKI, S. & THORODDSEN, S. T. 2012 von Kármán vortex street within an impacting drop. *Phys. Rev. Lett.* **108** (26), 264506.
- THORAVAL, M.-J., TAKEHARA, K., ETOH, T. G. & THORODDSEN, S. T. 2013 Drop impact entrapment of bubble rings. *J. Fluid Mech.* **724**, 234–258.
- THORODDSEN, S. T. 2002 The ejecta sheet generated by the impact of a drop. *J. Fluid Mech.* **451**, 373–381.
- THORODDSEN, S. T., ETOH, T. G., TAKEHARA, K., OOTSUKA, N. & HATSUKI, Y. 2005 The air bubble entrapped under a drop impacting on a solid surface. *J. Fluid Mech.* **545** (1), 203–212.
- THORODDSEN, S. T., THORAVAL, M.-J., TAKEHARA, K. & ETOH, T. G. 2011 Droplet splashing by a slingshot mechanism. *Phys. Rev. Lett.* **106** (3), 034501.
- VISSER, C. W., FROMMHOLD, P. E., WILDEMAN, S., METTIN, R., LOHSE, D. & SUN, C. 2015 Dynamics of high-speed micro-drop impact: numerical simulations and experiments at frame-to-frame times below 100 ns. *Soft Matter* **11**, 1708–1722.

- WAGNER, H. 1932 Über Stoß- und Gleitvorgänge an der Oberfläche von Flüssigkeiten. *Z. angew. Math. Mech.* **12**, 193–215.
- WILDEMAN, S., VISSER, C. W., SUN, C. & LOHSE, D. 2016 On the spreading of impacting drops. *J. Fluid Mech.* **805**, 636–655.
- WILSON, S. K. 1991 A mathematical model for the initial stages of fluid impact in the presence of a cushioning fluid layer. *J. Engg Math.* **25** (3), 265–285.
- YARIN, ALEXANDER L 2006 Drop impact dynamics: splashing, spreading, receding, bouncing. *Annu. Rev. Fluid Mech.* **38**, 159–192.
- ZHANG, L. V., TOOLE, J., FEZZAA, K. & DEEGAN, R. D. 2012*a* Evolution of the ejecta sheet from the impact of a drop with a deep pool. *J. Fluid Mech.* **690** (5), 5–15.
- ZHANG, L. V., TOOLE, J., FEZZAA, K. & DEEGAN, R. D. 2012*b* Splashing from drop impact into a deep pool: multiplicity of jets and the failure of conventional scaling. *J. Fluid Mech.* **703**, 402–413.
- ZHAO, R. & FALTINSEN, O. 1993 Water entry of two-dimensional bodies. *J. Fluid Mech.* **246** (1), 593–612.